8 Magnetic and related properties of silicates and phosphates

8.1 Silicates

8.1.1 Orthosilicates

(See Subvolume III/27I1)

8.1.2 Sorosilicates

8.1.2.1 Diorthopyrosilicates and related systems

The sorosilicate minerals from group VIII B01 are listed in Table 1 [91N1]. In addition, in this chapter, the synthetic silicates having the composition $R_2Si_2O_7$ where R is a rare-earth, Sc, Y or In as well as $Sm_4S_3Si_2O_7$, $La_4Se_3Si_2O_7$, $Ag_6Si_2O_7$ will be described. Keiviite and Thortveitite minerals contain a mixture of rare-earths, yttrium or scandium – Tables 1 and 3 – and thus their physical properties are dependent on composition which not in all cases is known. Consequently, we focus our attention mainly on the end series silicates.

8.1.2.1.1 Crystal structures. Lattice parameters

$R_2Si_2O_7$

The $R_2Si_2O_7$ silicates, where R is a rare-earth, yttrium, scandium or indium offer a typical example of polymorphism in connection with the ionic radius of R^{3+} cations, sintering temperatures or pressures. Structure investigations, at normal pressure, were performed [30Z1, 61L1, 62C1, 62L1, 64L1, 64W1, 65L1, 65T2, 67B1, 67B2, 67B3, 67S1, 68B1, 69F1, 69F2, 70B1, 70F1, 70F2, 70F3, 70S2, 70S3, 71F1, 72F1, 73F1, 73L1, 77B1, 82A1, 88B1, 90D1, 91G1, 94C1, 94C2, 97C1, 97C2, 00F1].

The polymorphisms shown by the *rare-earth disilicates*, elaborated at temperatures from 900°C to 1800°C and normal pressure, are presented in Fig. 1. Seven different types of structures were obtained, and were numbered from A to G [70F1]. Another classification was made according to their temperature increasing stability α(B)-β(C)-γ(D)-δ(E) [68I1]. Other polymorphs were then evidenced in R, Y, Sc, In disilicates as y-$Y_2Si_2O_7$ [62P1, 68I1, 72B1, 88D1], or those obtained under pressure X-$R_2Si_2O_7$ (R = Tm, Yb, Lu) with tetragonal structure or having cubic type structure as for R = Sc, In [77R1]. More recently a K-type, high-pressure structure, was reported for $R_2Si_2O_7$ (R = Nd, Sm, Eu, Gd) disilicates [01F1]. The projections of some representative crystal structures on different axes are shown in Fig. 2. The atomic coordinates are given in Table 2 and the lattice parameters are listed in Table 3. Some of their structures will be shortly presented below.

The acentric structure of the *low-temperature form of $Pr_2Si_2O_7$ (A-type)* consists of isolated $[Si_2O_7]^{6-}$ double tetrahedra and Pr^{3+} ions which are arranged in four sheets perpendicular to the ***c***-axis - Fig. 2a [71F1]. Within each of the four adjacent sheets, which are related through the 90° rotation of the 4_1-axis, the $[Si_2O_7]^{6-}$ units and the heavy atoms form rows running parallel the [110] direction. Within these rows always two of the double tetrahedra are closey related by a center of symmetry, the oxygen atoms forming some kind of closest packing. The heavy atoms are attached to each side of the sheets providing connection to the adjacent sheet. The anion

group $[Si_2O_7]^{6-}$ is free of symmetry restrictions since all atoms of the structure are in the general position. The tetrahedra pair is essentially of eclipsed configuration, but the ideal point symmetry mm2 is destroyed from a remarkable distortion of the tetrahedra bond lengths and angles especially of the second unit and from a twist angle about the Si–Si direction of each of the double tetrahedra. There is a rather irregular oxygen coordination of the Pr atoms with mixed coordination. Considering the dimensions of the Pr–O coordination polyhedra, the general impression is that the rare-earth ion seeks a compromise which will achieve spherical shielding for itself and minimize repulsion of the coordinating oxygen atoms [71F1].

The structure of the *high-temperature form of $Pr_2Si_2O_7$ (G-type)* is built up of columns containing the eclipsed double tetrahedra anion $[Si_2O_7]^{6-}$, packed with their "backbones" towards each other, but at alternating heights of *a*/2 - Fig. 2b [71F1]. Hence, the terminal oxygen atoms are found at the surface of columns. This arrangement leads to an eighfold oxygen coordination of both the heavy atoms. The Pr oxygen polyhedra in the shape of slightly distorted cubes are sharing edges parallel to [011], [01 $\bar{1}$] and [100] directions. Thus, twice the mean of the cube edge lengths meets precisely the value of the *a* dimension (5.40 Å) of the pseudo-orthorhombic but monoclinic unit cell.

The *β-$Yb_2Si_2O_7$(C)* crystallizes in space group C2/m. The structure of this phase is shown in Fig. 2c [70S2]. The numbers represent the approximate heights of atoms, expressed in hundredths of the ***c***-axis. The Yb octahedron is strongly distorted and has symmetry 2. Each Yb ion is coordinated to six oxygen atoms. The Si–O1–Si angle is 180°.

The *γ-$Er_2Si_2O_7$(D)* crystal is monoclinic having space group $P2_1/b$ [70S2]. The approximate values of *x* coordinates for atoms, as well as their environments are given in Fig. 2d. A striking feature of the silicate is that centrosymmetry of the Si_2O_7 group follows directly from the space group $P2_1/b$. Fourfold general positions and twofold special positions (on the centers of symmetry), are possible, in this space group. Since the unit cell contains only two pyrosilicate groups, they necessarily occupy these special positions. This structure provide evidence for the possibility of the existence of Si_2O_7 groups with a Si–O–Si angle of 180°. The terminal oxygen atoms of the pyrosilicate group form strongly distorted octahedra around the Er atoms similar to those around Yb in β-$Yb_2Si_2O_7$(C). The bridging oxygen atom O1 is not bonded to an erbium atom. Oxygen atoms of one polyhedron - Fig. 2d - belong to different pyrosilicate groups. Each octahedron is pointed to three other octahedra by common edges. As shown in Fig. 1, $Er_2Si_2O_7$ has three polymorphic forms for which the following sequence was established [68I1]: $\alpha \xrightarrow{1050(25)^\circ C} \beta \xrightarrow{1400(10)^\circ C} \gamma$.

The *δ-$Y_2Si_2O_7$(E)* is described in the space group Pnam with Y, O1 and O5 in the general 8d positions and the remaining atoms in the 4c special positions [90D1] – Table 2c. The numbering scheme given by [90D1] is identical to that used by [70S2] for the structure of $Gd_2Si_2O_7$ in the $Pna2_1$ space group, to facilitate comparison of the structures. For δ-$Y_2Si_2O_7$, however, O2 and O6 are related by symmetry to O1 and O5, respectively, and thus are absent from Table 2. As shown in Fig. 2e, Y has seven nearest neighbors O. These contacts are to five different Si_2O_7 groups, two below and three above Y as shown in the figure. Four of these groups provide one contact each but the fifth provides three contacts including one to the bridging O4. As a result, each terminal O is bonded to Si and to two Y. O4 is bonded to two Si and two Y. According to [72B1], y-$Y_2Si_2O_7$ shows a monoclinic structure. Later on, in [88D1] was reported that the structure is orthorhombic having space group Aba2.

The *B-type structure* , characteristic for $Dy_2Si_2O_7$, is build from a linear triple tetrahedral group $[Si_3O_{10}]$ and isolated $[SiO_4]$ tetrahedron cross-linked by Dy^{3+} in one sixfold and three eightfold coordinated positions - Fig. 2f1 – [00F1] and corresponds to revised type B structure of $Ho_2Si_2O_7$ [72F1]. The $Dy_2Si_2O_7$ crystal was complexly twinned such that the diffraction pattern was also consistent with a larger dimensionally monoclinic unit cell (a = 22.5354, b = 14.2102, c = 6.6158 Å, β = 91.788°), which resulted in an apparent superstructure of type B structure in space group C$\bar{1}$ [00F1]. Dy is accommodated in irregular coordination polyhedra, one sixfold polyhedra, Dy3 and three eightfold coordinated positions - Fig. 2f2. The nearest-neighbor environment of Dy4 is particularly irregular, approaching hemispherical, and backs onto a structural channel parallel to the ***b***-axis. Although all four Dy positions are coordinated to O atoms of both the silicate units, Dy2 and Dy3 principally cross-link the linear $[Si_3O_{10}]$ groups, whereas Dy1 and Dy4 interconnect isolated $[SiO_4]$ tetrahedra and terminal tetrahedra of the linear $[Si_3O_{10}]$ groups. The formation of the unusual linear triple tetrahedral group in the type B structure allows for a more continuous transition in the mean size of $R^{3+}O_n$ polyhedra through the 4f transition metal series.

A structure-type K - was reported for $R_2Si_2O_7$ (R = Nd, Sm, Eu, Gd) synthesized at 10 GPa and 1600…1700°C [01F1]. The omitting labels H and J from this series of rare-earth disilicate structure was caused by the fact that by J-phase was denoted YbN-woehlerite, $Yb_4Si_2O_7N_2$ [98I1] and H is used for hexagonal phase. The type K structure is built from a diorthosilicate group, Si_2O_7, interconnected by R^{3+} cations in eightfold coordination with oxygen - Fig. 2g. The bridging oxygen bond angle (Si–O–Si) of the diorthosilicate group of disilicates stable at 1 bar (A-G) is related to spatial accommodation of the R^{3+} cations and ranges from 130° to 135° in light R disilicates (A, F, G) to 180° in $Lu_2Si_2O_7$ (C). Volume reduction in the high pressure type K structure is achieved largely by closure of the Si–O–Si bond angle to 122.7°…124.4° through rigid body rotation of the two SiO_4 tetrahedra. This allows both of R^{3+} cations to be accommodated in eightfold coordinated polyhedra [01F1].

We note that other rare-earth disilicates show polymorphic transitions as $Ho_2Si_2O_7$ $\alpha \xrightarrow{1175(15)^\circ C} \beta \xrightarrow{1330(10)^\circ C} \gamma \xrightarrow{1475(25)^\circ C} \delta$ or $Tm_2Si_2O_7$ $\alpha \xrightarrow{1050(25)^\circ C} \beta$ [68I1] – see also Fig. 1.

According to [71F1], the polymorphism of a pyrosilicate is controlled by R atoms which request as much spherical shieldings as is allowed by the repulsion of the anion ligands. As the size of the R cation decreases, the repulsion between the ligands in the coordination shell increases and becomes large enough to make the structure energetically unstable. At this point, the coordination number of the R ion decreases and the crystal structure changes. Thus, the high number of disilicate polymorphs might be caused by the non-spherical shape of the complex anion $[Si_2O_7]^{6-}$. In order to meet requirements of the R cation, which has a highly electropositive character and strong polarizing forces, the anion offers essentially two different orientations. These are the staggered configuration of point symmetry $\bar{3}m$ (D_{3d}) in the sixfold coordinated R disilicates (types β(C) and γ(D)) and the eclipsed configuration of ideal point symmetry 2mm (C_{2v}), which is found in connection with the high coordination numbers 7, 8 and 9 in structure types δ(E), G and A, in several variations. The reversible transformation reported for $(La…Er)_2Si_2O_7$ at 1350(50)°C [69F2] was analyzed in correlation with the structural data of the representative disilicate $Pr_2Si_2O_7$ [71F1]. This is of reconstructive type and demands a considerable rearrangement of the cations and anion groups. Thus, the sheet-like structure, of the low-temperature form of $Pr_2Si_2O_7$, has to find the new arrangement, of back to backside packed double tetrahedra, ordered in columns, from the nearly closest packing in the sheets of the low form. The long diffusion lengths of the atoms determine the long time which had been observed for the transformation.

Analyzing the crystal structures of rare-earth disilicates, in [00F1, 01F1] was shown that in six of these structures (A, C, D, E, F and G), the SiO_4 tetrahedra are associated into diorthosilicate Si_2O_7 groups, and the structures essentially represent different ways of packing diorthosilicate groups and R^{3+} cations present in the ratio 1 : 2. The seventh structure type (B) which is adopted by disilicates with R = Eu, Gd, Tb, Dy, Ho, Er, at the lowest temperatures investigated (i. e., below 1000…1450°C) is unusual in having the SiO_4 tetrahedra in a one-to-one combination of a single (isolated) tetrahedron and a linear triple tetrahedral group Si_3O_{10}. The crystal chemistries of the R disilicates crystallized at 1 bar are constrained by the spatial accommodation of R^{3+} cations. For high-temperature disilicate structures the non-equivalent R^{3+} positions labeled by coordination number are: 6 (and near octahedral) in type C (Lu, Yb, Tm); 6 in type D (Er, Ho); 7 and 7 in type E (Ho, Dy, Tb, Gd, Eu); 7, 7, 8 and 8 in type F (Eu, Sm); and 8, 8 in type G (Sm, Nd, Pr, Ce, La); whereas, for moderate-temperature disilicate structures the coordinations are: 6 (and near octahedral) in type C (Lu, Yb, Tm, Er, Ho); 6, 8, 8, 8 in type B (Er, Ho, Dy, Tb, Gd, Eu) and 7, 7, 9, 9 in type A (Eu, Sm, Nd, Pr, Ce, La). In K-type structure the R^{3+} cations are in irregular eightfold and ninefold coordination. Above, the sequence of decreasing atomic number of R was used. The disilicate structures of the middle R are more complex and allow for a more progressive increase in polyhedral size, with a decrease in atomic number. This tendency is more exaggerated for the lower temperature phases [00F1]. Mean bond distances (≤ 2.8 Å [00F1] or ≤ 2.9 Å [01F1]) were compared with the effective bond distances for six-, seven-, eight- and ninefold coordination of R^{3+} with oxygen - Fig. 3. There are discontinuities representing the limits of accommodation of R^{3+} cations by individual structure types. There is tendency for structure types to define mean R–O bond distances, which tend to be greater than the sum of effective cation-anion radii given by [76S1] at the lower end of the cation size range of a given structure type and correspondingly smaller at the higher end.

Examination of the densities of the various rare-earths, $R_2Si_2O_7$, phases - Fig. 4 - shows that for Er- and Ho - disilicates, the β(C) form, is less dense than the γ(D) and α(B) forms, from which was inferred that the β(C) → γ(D) and β(C) → α(B) transformations should be induced by thermal treatment under pressure [77B1]. Really, a

study of the phase diagrams of $R_2Si_2O_7$ (R = Tm, Yb, Lu) shows extended polymorphism under high pressure [77B1]. The monoclinic γ(D) form appears at temperatures much lower than for the neighboring members of the series (above ≅ 900°C) and its stability fields is restricted to a narrow pressure range, around 20 kbar. The triclinic α(B) form appears at pressures which increase from 20 to 40 kbar from Tm to Lu, and temperatures which decrease when increasing pressure, generally higher than 800°C. A tetragonal X-form, isostructural with $Er_2Ge_2O_7$ one, was obtained at 25 kbar and 700°C [77B1]. Compared to the α(B) form it is a low-temperature, low-pressure form.

Yttrium disilicates, $Y_2Si_2O_7$, shows five (or possible six) structural forms (y, α, β, γ, δ and z). One of them, the yttrialite low form [62P1], so called y [72B1] is only stable up to 1200°C and can contain "stabilizing impurities" such as H^+, Na^+, Mg^{2+}, Mn^{2+}, Fe^{2+}, Fe^{3+}, Al^{3+}, Th^{4+} or Zr^{4+} [68I1, 69B1]. Then, it has been shown in the Y–Si–Al–O–N system that this phase can be obtained up to 1400°C [00P1]. The increase in the thermal stability could be due to stabilization of the y-structure, by impurities such as Al^{3+} and/or N^{3-}. The four other phases α(B), β(C), γ(D) and δ(E) were classified [68I1] according to their increasing stability with temperature, following the sequence $\alpha \xleftrightarrow{1225(10)^\circ C} \beta \xleftrightarrow{1445(10)^\circ C} \gamma \xleftrightarrow{1535(10)^\circ C} \delta$. Their structures, usually determined for members of the isostructural rare-earth compounds, are generally built up of $[Si_2O_7]^{6-}$ units linked by cations (y, β, γ, δ) and for α-structure, of $[Si_3O_{10}]^{8-}$ groups plus additional $[SiO_4]^{4-}$ tetrahedra. The X-ray diffraction of a single crystal α-$Ho_2Si_2O_7$ has shown four silicon environments and Si–O–Si bond angles of 118.2° and 133.2° [73F1]. For y-$(Th,Y)_2Si_2O_7$, the same technique has shown two silicon sites and a bond angle of 134° [72B1]. The δ-$Y_2Si_2O_7$ phase exhibits two sites and a bond angle of 158° [70S2, 73F1, 97C1]. For β and γ, a single silicon site was observed for rare-earth and yttrium disilicates, respectively, and space-group considerations predict a bond angle of 180° [70S2, 73F1]. In [97C1] was reported a value of 172° for the γ-$Y_2Si_2O_7$ phase. Another form z-$Y_2Si_2O_7$ has been reported only once [68I1], with an unindexed powder diffraction pattern. This phase seems to be a low-temperature form, stable only below 1030°C.

The oxinitride R–Si–Al–O–N phases, where R is a rare-earth or yttrium [88D1, 93T1], have generated a revival of interest of phase transformations in the $Y_2Si_2O_7$ system. In [00P1] was shown that some of their forms appear in Si_3N_4 grain boundaries, often as a secondary phase, in the synthesis of R–Si–Al–O–N compounds, either in the as prepared state or after oxidation [00P1]. Differences in the polymorph stability ranges were noticed [97L1] compared to the sequence given by [68I1]. This could be due to the origin of the sample and /or the presence of impurities stabilizing one polymorph relative to another. In [00P1] different polymorphs of $Y_2Si_2O_7$ have been synthesized by a sol-gel (SG) process and by mixed powder (MP) routes. In [88D1] the crystallization of Y_2O_3-SiO_2-AlN glasses was analyzed. The ranges of stability were discussed as function of heat treatment and synthesis route. The amorphous SG samples were obtained after calcination at 600°C. At 1060°C a crystallization to α-phase was shown [00P1]. Treatments, below this temperature, yielded y- or α-phases according to calcination time. The y form (usually only obtained in the presence of impurities) is possibly stabilized by residual hydroxyl groups present at this temperature. A longer heat treatment time promotes the formation of α by removing these hydroxyl groups. The poor crystallinity of y-$Y_2Si_2O_7$ is related to the low preparation temperature. For this phase, different indexing were given: monoclinic $P2_1/m$ [72B1, 86L2] or orthorhombic Aba2 [88D1]. The α form was the main phase observed at 1200°C. Longer calcination time (24 h) was necessary to obtain the transformation of the α- to higher temperature forms in relation to the low rate of reconstruction of the crystalline structure. The phase transformations follow the sequence $\alpha \rightarrow \beta \rightarrow \gamma$. The slow kinetics, probably, explain why the δ -form was not observed even at 1600°C. This phase formed more easily by solid state reaction between Y_2O_3 and SiO_2 , at 1700°C. The γ form appeared on calcination at 1350°C, instead at 1450°C reported in [68I1]. The β-phase appeared at 1300°C and was always present after quenching from higher temperatures (1600°C).

The crystallization of Y_2O_3–SiO_2–AlN system was found to proceed by heterogeneous nucleation mechanism with intermetallic iron silicides acting as nuclei for columnar dendritic y-$Y_2Si_2O_7$ species [88D1]. Secondary crystallization, of a species having a nominal composition of $YSi_2AlO_4N_2$, occurred in interdendritic regions when the crystallization temperature approached 1200°C. A third stage of crystallization involved the formation of the high- temperature polymorph of $Y_2Si_2O_7$ (δ_2-$Y_2Si_2O_7$), through transformation of the y-$Y_2Si_2O_7$ dendrites to an intermediate product (δ_1-$Y_2Si_2O_7$) followed by recrystallization to the δ_2-$Y_2Si_2O_7$ polymorph. According to

[88D1], the δ_2-$Y_2Si_2O_7$ is based on a primitive orthorhombic lattice having space group $Pna2_1$ (a =13.6 Å, b = 5.01 Å, c = 8.15 Å).

The $Sc_2Si_2O_7$ and $In_2Si_2O_7$ have been converted from the thortveitite-type structure to pyrochlore-type at 1000°C and 120 kbar [77R1]. The pyrochlore $A_2B_2O_7$ structure, can be considered [65K1, 68H1] to be derived from that of fluorite, with the cubic fluorite axis doubled to allow A and B atoms to alternate in the fluorite metal atom sites, and with one-eighth of the oxygen atoms missing. The structure is thus characterized by a set of AO_8 polyhedra formed from distorted cubes corner-joined through O1 atoms to form a network which is interpenetrated by a network of symmetrically distorted corner-joined BO_6 octahedra in which the B–O bonds are of equal length. Each O1 is at the center of a regular tetrahedron of A atoms and the O2 atoms are also four coordinated, with two bonds to A atoms and two to B atoms. The atomic coordinates for cubic $A_2Si_2O_7$ (A = Sc, In) are given in Table 2h. Pyrochlore phases were not produced from rare-earth disilicate or monosilicate phases, subjected to the same reaction conditions as the Sc and In compounds.

Crystals of pyrosilicate type were grown by several methods. Thus, single crystals of $Yb_2Si_2O_7$ [68B2], $Er_2Si_2O_7$ [74W1, 78W1] and $R_2Si_2O_7$ (R = Dy, Ho, Er, Tm) [79M1] were obtained by crystallization from a molten mixture. $Y_2Si_2O_7$ crystals were grown by hydrothermal method [68I1] and $R_2Si_2O_7$ (R = Nd, Gd, Er. Yb) crystals by Verneuil method [70S2]. Growing of rare-earth, yttrium and scandium pyrosilicate crystals by the Czochralski method was also reported [82A1]. In [72B1] y-$Y_2Si_2O_7$ crystals were obtained in an electric arc.

$Sc_2Si_2O_7$–$Y_2Si_2O_7$

The $(Sc_{1-x}Y_x)_2Si_2O_7$ silicates, having monoclinic C2/m-type structure, form solid solutions in all the composition range. The composition dependences of the lattice parameters are given in Fig. 5 [68I1].

Gittinsite, $CaZrSi_2O_7$

The crystal structure of gittinsite was reported to be monoclinic. Initially, the space group C2/m was considered [80A1]. Then, it has been shown that the crystal structure has the space group C2 and consists of octahedral sheets that are one third filled with calcium, one third filled with zirconium and one third vacant [89R1]. The sheets are separated by Si_2O_7 groups, producing a void in the center of the unit cell - Fig. 6 [89R1]. The calcium-oxygen octahedra share three edges with the zirconium-oxygen octahedra and three edges with the octahedral voids to form the octahedral layer. Likewise, the octahedral voids share three edges with zirconium-oxygen octahedra. These voids show an irregular octahedral coordination. The unoccupied site is octahedrally coordinated. The atomic sites are listed in Table 2.

The crystal structure of gittinsite is a modification of the thorveitite structure. Both structures contain isolated Si_2O_7 groups. In gittinsite, the edge sharing calcium-oxygen and zirconium-oxygen octahedra form sheets parallel to the (001) plane, which are connected by Si_2O_7 groups located above and below a void centered at 0.5, 0.5, 0.5. Differences between the gittinsite and thorveitite structures are the result of the replacement of the two Sc^{3+} atoms in thorveitite by the Ca^{2+} and Zr^{4+} atoms in gittinsite. In thortveitite (C2/m), the Sc sites are equivalent and Si–O–Si angle is 180°, whereas in gittinsite (C2) – the bridging angle is 147.4(5)°.

$Sm_4S_3Si_2O_7$, $La_4Se_3Si_2O_7$

$Sm_4S_3Si_2O_7$ crystallizes in a tetragonal structure of $I4_1/amd$ space group [82S1]. The structure contains two kinds of Sm atoms. Sm1 is coordinated to three O and three S atoms and Sm2 to six O and three S atoms. The $[Si_2O_7]$ double tetrahedra are in the eclipsed configuration. A non-centrosymmetric eclipsed configuration similar to the one in $Sm_4S_3Si_2O_7$ was also found in type A ($Sm_2Si_2O_7$) [70S3], type δ(E) ($Eu_2Si_2O_7$) and type G ($Pr_2Si_2O_7$) pyrosilicates.

$La_4Se_3Si_2O_7$ crystallizes also in a tetragonal symmetry, space group $I4_1/amd$ [93D1]. The structure contains isolated $[Si_2O_7]$ units (double tetrahedra) which are formed by condensation of two $[SiO_4]$ tetrahedra connected by a sharing corner. These $[Si_2O_7]$ units bridge all other polyhedra built around two kinds of lanthanum atoms. La1 is coordinated to three O and three Se atoms while La2 is coordinated by six O and three Se atoms.

It seems that a larger family of compounds could be made by substituting La or Sm by other rare-earth elements for sulfide and selenide derivatives [93D1].

$Ag_6Si_2O_7$

The silicate crystallizes in a monoclinic structure having P2/n space group [77J1]. Bond lengths and angles of $Si_2O_7^{6-}$ are in agreement with those in other disilicates.

8.1.2.1.2 Magnetic properties

γ-$Er_2Si_2O_7$(D)

The temperature dependences of the magnetic susceptibilities carried along the ***a***- and ***c***-axes of a single crystal and along the ***m***-axis, which corresponds to the direction of maximum susceptibility in the (*ab*) plane, determined to be at 28° to the ***a***-axis, are plotted in Fig. 7. The ***a***- and ***c***-axis susceptibilities display considerably anisotropy and also evidence an antiferromagnetic transition around 1.9 K [86L1].

The magnetic anisotropy of the Er^{3+} ground state, in γ-$Er_2Si_2O_7$(D), was investigated by optical absorption spectroscopy. The spectum, in the visible region, contains several sharp lines corresponding to Er^{3+} electronic transitions. The one chosen for detailed study was the lower energy one of the two transitions from the ground state (GS) to $^4S_{3/2}$, at 547 nm. Since Er^{3+} is a Kramers ion, all states are doublets with effective spin $S' = 1/2$ and Zeeman splittings are characterized by an anisotropic g value (g_{lmn}): $\Delta\nu = g_{lmn}\mu_B B$, where $g_{lmn} = (g_x l^2 + g_y m^2 + g_z n^2)$ and l, m, n are the cosines of the field direction to the principal axes of the **g**-tensor: x, y, z. A maximum g value was observed for two directions: 15° above and 15° below the (*ab*) plane. For Er^{3+} ion, the local ***z***-axis was chosen in the direction of maximum moment and the local x-axis is in the (*ab*) plane. From the analysis of angular Zeeman spectra, the principal g values $g_x = 13.4(3)$; $g_y = 3.4(6)$ and $g_z = 2.6(3)$ were obtained. The Er^{3+} ground state magnetic moment, therefore, lies predominantly in the ***z***-direction. The magnetically ordered state was interpreted in terms of four-sublattice antiferromagnetic arrangements of Ising-like moments - Fig. 8.

The field dependences of the magnetic moments along both the ***a*** and ***m*** directions (Fig. 9a) and at 55° from ***m***-axis, in the (***m***, ***c***) plane (Fig. 9b) are typical for a metamagnetic transition. For low fields, the moments are close to zero, while for a critical field, whose value is related to the strength of the inter-ionic interactions, the moments increase rapidly as the sublattices, initially antiparallel to the applied field, begin reversing their direction in order to minimize their energy. For fields applied in the ***a*** and ***m*** directions, there is a step in the steeply rising portion at about one third of the saturation value. The possible existence of various intermediate and final states of the magnetic order, as a function of external field, was analysed. On this basis, the phase diagram at $T = 0$ K was determined - Fig. 10. If the angle θ in the (*ab*) plane is $\theta = 45°…75°$, when increasing the external field, the system passes through all four phases and three phase transitions are expected to be seen. The field dependences of the magnetic moments p_A at 0.5 K, for $\theta = 55°$, are shown in Fig. 9b. Three well defined regions in which the p_A vs B dependence is linear, and a fourth region approaching to magnetic saturation at the highest fields were shown. We note that the demagnetizing effects were not considered. This may explain the discrepancies between the experimental values and those expected from the phase diagram - Fig. 10.

By using the results of magnetic measurements and the data obtained from Zeeman spectra, the exchange interactions were determined. The computed exchange interactions between an ion on sublattice 1 interacting with ions on sublattices 1…4 are shown in Table 4 [86L1]. The exchange interaction, in each case, is assumed to be within NN ion on each sublattice. Since there are two NN ions on sublattices 2 and 3, these energies need to be halved to give the individual NN interactions.

The results of calculation of the temperature dependence of the sublattice magnetization and the magnetic susceptibilities in the ***m*** direction, based on the exchange interaction constants (Table 4) are given in Fig. 11. The agreement between the χ vs T experimentally determined values and those computed is rather good. We note that the calculated value of 0.44 is higher than 1/3 step in the magnetization measured as function of the field along the ***a*** and ***m***-axes. It was suggested that a larger unit cell with twelve magnetic sublattices may be considered in order to obtain a better agreement with experimental data [86L1].

8.1.2.1.3 Nuclear magnetic resonance (NMR) data

$R_2Si_2O_7$ (R = Y, La)

The first ^{29}Si MAS NMR spectra studies were those of γ-$Y_2Si_2O_7$(D) and δ-$Y_2Si_2O_7$(E) forms [84G1], but the two peaks for the δ-phase were hardly resolved. It was suggested that increasing bond angles cause high-field ^{29}Si chemical shift. In [87S1] some relatively broad spectra were recorded for α(B)-, β(C)-, γ(D)- and δ(E)-$Y_2Si_2O_7$. For δ(E)-$Y_2Si_2O_7$ silicate, the two peaks were still scarcely distinguished and for α-$Y_2Si_2O_7$(B) only one broad peak was observed. In addition, the spectra exhibit spinning sidebands, which were attributed to the chemical shift anisotropy. Other measurements for β-$Y_2Si_2O_7$(C) and γ-$Y_2Si_2O_7$(D) were also reported [88D2, 91K1]. In Fig. 12 are plotted the resolved ^{29}Si MAS NMR spectra for the phases α(B)-, β(C)-, γ(D)- and δ(E)-$Y_2Si_2O_7$ [00P1] and in Table 5 the determined parameters. For all forms, peaks corresponding to each silicon site in the crystal structure (i.e. 4 for α(B)-, 2 for δ(E)-, 1 for β(C)- and γ(D)-) were resolved. The lower chemical shift for Q^1 silicon environments in β(C)- and γ(D)-forms, compared with those of α(B)- and δ(E)-, were correlated with the Si–O–Si bond angles which are larger in β(C) (180°) and γ(D) (172°) than in α(B) (132.2° and 118.2°) and δ(E) (158°) phase [70S2, 73S1]. The same correlation may explain the slight difference in chemical shift between the β(C)- and γ(D)-forms. The different silicon environments of α(B)-form (Q^0, Q^1, Q^2) give signals nearby at the same chemical shifts and were difficult to be assigned. In [00P1] was suggested that extreme high- and low-frequency peaks arise from Q^0 and Q^2 sites, respectively, and that the middle two signals may be assigned to Q^1 silicon.

The ^{29}Si MAS NMR study was performed in β(C)-$La_2Si_2O_7$ [88D2, 89H1] - Table 5. An environment Q^1 was proposed.

8.1.2.1.4 Optical properties

γ-$Er_2Si_2O_7$(D)

The Zeeman spectra of Er^{3+} ($^4I_{15/2}GS \rightarrow {}^4S_{3/2}$ lower component), at 0.7 K, as function of applied field are shown in Fig. 13 [86L1]. In zero field, at $T > T_N$, in the 547 nm wavelength region, one observes two lines corresponding to transitions from the ground state to the two levels in $^4S_{3/2}$. As temperature is lowered below T_N, this single spectral line begins to display splittings that can be attributed to an "internal" Zeeman effect caused by the interaction of both the ground state and the optically excited state of a single ion, with the internal fields arising from the onset of magnetic order. Further splitting occurs (giving lines a, b, c, d) as the field is applied, because those sublattices, whose moments are parallel to the field, are no longer equivalent to those sublattices whose moments are antiparallel. The spectrum is confused in the spin-flip regions but above 0.75 T, when the saturation was nearly obtained, is present a strong pair of lines e, f and the corresponding but steadily weakening pair, g, h. Thus, for fields greater than the critical field, all ions are equivalent and both e, f and g, h splittings are due to the optically excited states. The lines g, h originate on the rapidly decreasing number of sites where the ground-state moment is still antiparallel to the applied field. Their intensity goes to zero at 0.85 T when the total moment reaches saturation - Fig. 9. The center of gravity of the four lines e, f, g, h should correspond to the energy of the transition in the complete absence of internal or external fields. The difference between this value and the center of gravity of the two lines in zero field gives the magnetic energy of an ion in the antiferromagnetic state, $E_a = 2.39(5)$ cm^{-1}. This value is somewhat higher than $E_a' = 2.15(5)$ cm^{-1} obtained as the difference between the line position at $T > T_N$ and the average of the pair (the excited – state splitting) observed at 0.7 K.

$R_2Si_2O_7$ (R = Lu, In, Sc, Yb)

The infrared (IR) spectra of $Lu_2Si_2O_7$ and $In_2Si_2O_7$, having C2/m type structure, were measured in the frequency range 1300…400 cm^{-1} - Fig. 14 [81O1]. The frequencies of the anti-symmetrical Si–O–Si stretching for R = In and Lu are at 1175 cm^{-1} and 1115 cm^{-1}, respectively. Values of 1169 cm^{-1} for $Sc_2Si_2O_7$, and 1110 cm^{-1} in case of $Yb_2Si_2O_7$, were obtained [71L1]. The frequencies of ν_{as} Si–O–Si vary linearly with the electronegativities of R^{3+} ions. This suggests that the Si–O (br) distances in thortveititie structure (C2/m-type) is strongly influenced by R^{3+} ions [81O1].

Normal coordinate calculations have been carried on $Sc_2Si_2O_7$ [87D1]. The simulated spectrum describes well the experimentally recorded one [65T1].

The Raman spectra of pyrosilicates were studied by [73T1].

Refractive indices for some pyrosilicates are given in Table 6.

Tables and figures

Table 1. Silicate minerals from group VIIIB01 [91N1] as well as related synthetic silicates.

Mineral	Silicate	Group
Thortveitite	$(Sc,Y)_2Si_2O_7$	VIIIB01
Keiviite (Y)	$(Y,Yb)_2Si_2O_7$	VIIIB01
Keiviite (Yb)	$(Yb,Y)_2Si_2O_7$	VIIIB01
Gittinsite	$CaZrSi_2O_7$	VIIIB01
Rowlandite	$FeY_4(Si_2O_7)F_2$	VIIIB01
Synthetic silicates:	$R_2Si_2O_7$ [1)]	
	$Sm_4S_3Si_2O_7$	
	$La_4Se_3Si_2O_7$	
	$Ag_6Si_2O_7$	

[1)] R is a rare earth, Sc, Y or In.

Table 2. Atomic sites and thermal parameters.

a) β-$Yb_2Si_2O_7$ (C) having C2/m space group [70S3].

Atom	*x*	*y*	*z*	B_{eq} [Å^2]
Yb	1/2	0.80687(2)	0	0.25
Si	0.7189(3)	1/2	0.4125(6)	0.37
O1	1/2	1/2	1/2	1.02
O2	0.8831(5)	1/2	0.7151(15)	0.50
O3	0.7361(5)	0.6504(4)	0.2197(11)	0.54

b) γ-$Er_2Si_2O_7$ (D) having $P2_1/b$ space group [70S3].

Atom	*x*	*y*	*z*	B_{eq} [Å^2]
Er	0.88829(8)	0.09318(6)	0.34934(5)	0.29
Si	0.3601(4)	0.6442(3)	0.3871(3)	0.33
O1	1/2	1/2	1/2	0.91
O2	0.2052(8)	0.8653(7)	0.4486(6)	0.64
O3	0.1235(9)	0.4583(8)	0.3191(6)	0.63
O4	0.6184(9)	0.7522(7)	0.2984(6)	0.56

c) δ-$Y_2Si_2O_7$ (E) having orthorhombic structure, space group Pnam [90D1].

Atom	*x*	*y*	*z*	B_{eq} [Å^2]
Y	0.1255(2)	0.3395(4)	–0.0096(2)	0.12(1)
Si1	0.3179(7)	0.3711(21)	1/4	0.14(2)
Si2	0.5410(7)	0.6214(9)	1/4	0.10(2)
O1	0.2671(11)	0.4875(30)	0.0861(16)	0.09(3)
O3	0.3476(17)	0.0613(54)	1/4	0.18(6)
O4	0.4218(14)	0.5588(44)	1/4	0.02(5)
O5	0.5477(13)	0.7994(31)	0.0817(17)	0.18(4)
O7	0.6031(19)	0.3386(55)	1/4	0.22(6)

Table 2 (continued)

d) $Pr_2Si_2O_7$ (A) having $P4_1$ space group [71F1].

Atom	*x*	*y*	*z*	B_{eq} [Å^2]
Pr1	0.7665(3)	0.2970(3)	0.9929(4)	0.78(7)
Pr2	0.5205(3)	0.1663(3)	0.1407(4)	0.89(8)
Pr3	0.3376(3)	0.9180(3)	0.9931(4)	0.76(7)
Pr4	0.1219(3)	0.7632(3)	0.1325(4)	0.91(8)
Si1	0.8559(12)	0.7601(11)	0.0099(5)	0.52(14)
Si2	0.5999(2)	0.6954(11)	0.1094(5)	0.48(15)
Si3	0.2626(11)	0.3770(11)	0.0149(5)	0.43(14)
Si4	0.0099(11)	0.2913(12)	0.1153(5)	0.55(16)
O1	0.893(3)	0.615(2)	0.959(1)	0.59(23)
O2	0.726(3)	0.933(2)	0.984(1)	0.63(24)
O3	0.047(3)	0.840(3)	0.041(1)	0.83(31)
O4	0.719(3)	0.628(3)	0.052(1)	1.02(36)
O5	0.482(2)	0.523(3)	0.135(1)	0.81(29)
O6	0.434(3)	0.848(3)	0.091(1)	0.92(28)
O7	0.748(2)	0.818(3)	0.147(1)	0.67(23)
O8	0.322(3)	0.570(2)	0.988(1)	0.84(23)
O9	0.454(3)	0.236(2)	0.036(1)	0.77(24)
O10	0.134(2)	0.250(3)	0.976(1)	0.94(31)
O11	0.120(2)	0.427(2)	0.065(1)	1.68(49)
O12	0.968(2)	0.458(2)	0.160(1)	0.89(34)
O13	0.160(2)	0.127(2)	0.140(1)	1.11(30)
O14	0.815(2)	0.205(3)	0.089(1)	0.64(19)

e) $Pr_2Si_2O_7$ (G) having $P2_1/n$ space group [71F1].

Atom	*x*	*y*	*z*
Pr1	0.52097(12)	0.80685(7)	0.76857(4)
Pr2	0.84809(13)	0.60513(7)	0.59012(4)
Si1	0.07968(6)	0.02473(3)	0.00252(2)
Si2	0.09085(6)	0.04964(3)	0.01789(2)
O1	0.08324(15)	0.04220(8)	0.00643(5)
O2	0.00713(16)	0.01434(8)	0.00043(22)
O3	0.05749(16)	0.01548(9)	0.00534(5)
O4	0.07403(16)	0.02391(9)	0.09060(5)
O5	0.07441(15)	0.04167(8)	0.02403(5)
O6	0.02216(16)	0.04744(9)	0.02477(5)
O7	0.08192(17)	0.06747(9)	0.01724(5)

Table 2 (continued)

f) $Dy_2Si_2O_7$ (B) having triclinic structure, space group $P\bar{1}$ [00F1].

Atom	*x*	*y*	*z*	U_{eq} [Å^2] · 10^3
Dy1	0.94853(4)	0.33132(4)	0.11643(2)	5.88(9)
Dy2	0.88556(4)	0.09387(4)	0.35971(2)	5.79(9)
Dy3	0.37254(4)	0.78116(4)	0.36895(2)	7.49(9)
Dy4	0.66787(4)	0.82973(4)	0.10747(2)	7.42(9)
Si1	0.1553(2)	0.8528(2)	0.1164(1)	4.8(3)
Si2	0.4873(3)	0.3370(2)	0.1759(1)	6.1(3)
Si3	0.3777(3)	0.2743(2)	0.4048(1)	6.4(3)
Si4	0.1433(3)	0.3702(2)	0.6180(1)	5.6(3)
O1	0.6418(6)	0.4938(6)	0.1256(3)	7.6(7)
O2	0.6179(7)	0.1419(6)	0.2095(4)	12.0(8)
O3	0.2978(7)	0.2990(7)	0.0947(3)	9.7(8)
O4	0.4055(6)	0.4283(6)	0.3065(3)	7.2(7)
O5	0.5836(7)	0.1702(6)	0.4454(4)	9.0(8)
O6	0.2276(6)	0.0965(6)	0.3755(4)	10.0(8)
O7	0.2885(7)	0.4229(6)	0.5118(3)	9.3(8)
O8	0.2841(7)	0.2167(7)	0.6875(4)	11.8(8)
O9	0.9629(7)	0.2255(6)	0.5700(4)	11.3(8)
O10	0.0732(7)	0.5777(6)	0.6854(4)	10.9(8)
O11	0.2411(7)	0.9129(7)	0.9994(3)	11.1(8)
O12	0.3462(6)	0.7886(7)	0.1888(4)	9.5(8)
O13	0.9982(6)	0.6683(6)	0.0809(3)	7.7(8)
O14	0.0029(6)	0.0165(6)	0.1830(3)	7.5(7)

g) $Nd_2Si_2O_7$ (K) having monoclinic structure, space group $P2_1/n$ [01F1].

Atom	*x*	*y*	*z*	B_{eq} [Å^2]
Nd1	0.17108(4)	0.89475(4)	0.63907(2)	0.671(6)
Nd2	0.20339(4)	0.68497(4)	0.34238(2)	0.718(6)
Si1	0.6901(2)	0.8258(2)	0.5854(1)	0.47(2)
Si2	0.6877(2)	0.5745(2)	0.3931(1)	0.58(2)
O1	0.5719(4)	0.7135(5)	0.4711(3)	0.73(6)
O2	0.8268(4)	0.0070(4)	0.5492(3)	0.55(5)
O3	0.8350(4)	0.7163(4)	0.3362(3)	0.65(6)
O4	0.5040(5)	0.5041(5)	0.2925(3)	0.82(6)
O5	0.5375(5)	0.9176(4)	0.6563(3)	0.69(6)
O6	0.8535(5)	0.6736(5)	0.6581(3)	0.86(6)
O7	0.8019(5)	0.3910(5)	0.4634(3)	0.75(6)

Table 2 (continued)

h) $A_2Si_2O_7$ (A = Sc, In) having cubic Fd3m space group [77R1].

Atom	Site	*x*	*y*	*z*
Sc (In)	16c	0	0	0
Si	16d	1/2	1/2	1/2
O1	8a	1/8	1/8	1/8
O2	48f	*x*[1)]	1/8	1/8

[1)] $x = 0.4313(21)$ for A = Sc and $x = 0.4272(15)$ for A = In.

i) Gittinsite having C2 space group [89R1].

Atom	*x*	*y*	*z*	$\beta_{ij} \cdot 10^3$					
				β_{11}	β_{22}	β_{33}	β_{12}	β_{13}	β_{23}
Zr	0.0000	0.3140(2)	0.5000	10.3(2)	9.9(4)	9.6(3)	0	1.5(5)	0
Ca	0.0000	0.7063(2)	0.5000	17.9(9)	10.4(8)	27(1)	0	–14(2)	0
Si	0.2123(2)	0.9920(2)	0.9187(4)	12.8(7)	12.6(8)	8.6(7)	2(1)	–1(1)	–1(2)
O1	0.0000	0.9387(9)	0.0000	13(2)	29(4)	27(4)	0	7(6)	0
O2	0.3734(6)	0.0000	0.2196(10)	16(2)	16(2)	12(2)	1(3)	–8(3)	2(6)
O3	0.1885(8)	0.1549(6)	0.7405(11)	30(2)	12(2)	15(2)	1(6)	–6(5)	1(4)
O4	0.2640(7)	0.8539(5)	0.7103(0)	21(2)	16(4)	13(2)	–4(3)	5(5)	–9(4)

Table 3. Crystal structures and lattice parameters at RT.

Silicate	Space group	Lattice parameters				Refs.
		a [Å]	*b* [Å]	*c* [Å]	α, β, γ	
Thortveitite[1)]	C2/m	6.650(1)	8.616(1)	4.686(1)	$\beta = 102.20(1)°$	88B1
Thortveitite[2)]	C2/m	6.587(1)	8.547(1)	4.695(1)	$\beta = 102.65(1)°$	88B1
Thortveitite[3)]	C2/m	6.582(1)	8.555(1)	4.693(1)	$\beta = 102.59(1)°$	88B1
Thortveitite[4)]	C2/m	6.527(8)	8.507(1)	4.691(1)	$\beta = 102.78(1)°$	88B1
Thortveitite[5)]	C2/m	6.542(5)	8.519(5)	4.669(5)	$\beta = 102°33(10)'$	62C1
β-$Sc_2Si_2O_7$(C)	C2/m	6.503(2)	8.498(3)	4.682(2)	$\beta = 102.77(7)°$	72S1, 73S1
β-$Sc_2Si_2O_7$(C)	C2/m	6.52	8.51	4.68	$\beta = 102.7°$	68I1
β-$Sc_2Si_2O_7$(C)	C2/m	6.542(5)	8.519(5)	4.669(5)	$\beta = 102°33(10)'$	70S1
β-$Sc_2Si_2O_7$(C)	C2/m-C2-Cm	6.502(2)	8.502(2)	4.684(2)	$\beta = 102.69(2)°$	82A1
$Sc_2Si_2O_7$[6)]	Fd3m	9.287(3)				77R1
$La_2Si_2O_7$(G)	$P2_1/n$	8.794(2)	13.201(2)	5.409(1)		69F2
$La_2Si_2O_7$(G)	$P2_1/n$	8.790(3)	13.163(7)	5.389(9)		82A1
$La_2Si_2O_7$(G)	$P2_12_12_1$	5.410(5)	13.17(2)	8.76(1)		70S2
$La_2Si_2O_7$(A)	$P4_122$-$P4_1$	6.7945(9)		24.871(8)		69F2
$Ce_2Si_2O_7$(G)	$P2_12_12_1$	5.400(5)	13.05(2)	8.73(1)		70S2
$Ce_2Si_2O_7$(G)	$P2_1/n$	8.721(5)	13.075(8)	5.405(6)		82A1
$Ce_2Si_2O_7$(G)	$P2_1/n$	8.722(1)	13.056(2)	5.401(1)		70F1

Table 3 (continued)

Silicate	Space group	Lattice parameters				Refs.
		a [Å]	*b* [Å]	*c* [Å]	α, β, γ	
$Pr_2Si_2O_7$(A)	$P4_122$-$P4_1$	6.7657(6)		24.608(4)		69F2
$Pr_2Si_2O_7$(A)	$P4_1$	6.769(1)		24.607(5)		71F1
$Pr_2Si_2O_7$(G)	$P2_1/c$	5.407(1)	8.679(1)	12.990(2)	$\beta = 90.00(1)°$	71F1
$Pr_2Si_2O_7$(G)	$P2_1/n$	8.670(3)	12.985(6)	5.397(8)		82A1
$Pr_2Si_2O_7$(G)	$P2_1/n$	8.674(1)	12.996(2)	5.405(1)	$\beta = 90.0°$	69F2
$Nd_2Si_2O_7$(A)	$P4_122$-$P4_1$	6.7405(6)		24.524(4)		69F2
$Nd_2Si_2O_7$(G)	$P2_1/n$	8.630(2)	12.945(2)	5.391(1)	$\beta = 90.0°$	69F2
$Nd_2Si_2O_7$(G)	$P2_1/n$	8.625(2)	12.939(4)	5.392(4)		82A1
$Nd_2Si_2O_7$(G)	$P2_12_12_1$	5.394(5)	12.95(1)	8.72(1)		70S3
$Nd_2Si_2O_7$(K)	$P2_1/n$	6.6658(2)	6.7234(3)	12.3975(6)	$\beta = 102.147(3)°$	01F1
$Sm_2Si_2O_7$(A)	$P4_122$-$P4_1$	6.6933(8)		24.384(9)		69F2
$Sm_2Si_2O_7$(A)	$P4_1$	6.695(5)		24.40(2)		70S3
$Sm_2Si_2O_7$(G)	$P2_1/n$	8.564(7)	12.855(9)	5.383(5)		69F2
$Sm_2Si_2O_7$(G)	$P2_12_12_1$	5.384(5)	12.85(2)	8.69(1)		70S2
$Sm_2Si_2O_7$(F)	$P\bar{1}$-P1	8.513(3)	12.867(4)	5.374(2)	$\alpha = 91.34(3)°$ $\beta = 92.06(4)°$ $\gamma = 90.43(3)°$	70F1
$Sm_2Si_2O_7$(K)	$P2_1/n$	6.6039(3)	6.6849(3)	12.3069(5)	$\beta = 102.489(3)°$	01F1
$Eu_2Si_2O_7$(A)	$P4_122$-$P4_1$	6.6727(7)		24.338(3)		69F2
α-$Eu_2Si_2O_7$(B)	$P\bar{1}$-P1	6.716(3)	6.762(3)	12.321(7)	$\alpha = 94.36(4)°$ $\beta = 90.02(3)°$ $\gamma = 91.75(4)°$	70F1
$Eu_2Si_2O_7$(F)	$P\bar{1}$-P1	8.517(1)	12.848(2)	5.385(1)	$\alpha = 91.65(2)°$ $\beta = 92.24(2)°$ $\gamma = 90.44(2)°$	70F1
δ-$Eu_2Si_2O_7$(E)	Pnma-$Pna2_1$	13.9142(9)	5.0553(4)	8.3486(7)		70F1
$Eu_2Si_2O_7$(G)	$P2_12_12_1$	5.374(5)	12.82(2)	8.65(1)		70S2
$Eu_2Si_2O_7$(K)	$P2_1/n$	6.5777(3)	6.6652(4)	12.2668(8)	$\beta = 102.671(4)°$	01F1
α-$Gd_2Si_2O_7$(B)	$P\bar{1}$-P1	6.624(5)	6.679(5)	12.132(9)	$\alpha = 94.10(8)°$ $\beta = 89.79(9)°$ $\gamma = 91.60(7)°$	70F1
δ-$Gd_2Si_2O_7$(E)	Pnam-$Pna2_1$	13.8665(9)	5.0532(4)	8.3008(8)		70F1
δ-$Gd_2Si_2O_7$(E)	Pnam-$Pna2_1$	13.846(5)	5.049(2)	8.292(1)		82A1
δ-$Gd_2Si_2O_7$(E)	$Pna2_1$	13.870(15)	5.073(5)	8.33(1)		70S2
$Gd_2Si_2O_7$(K)	$P2_1/n$	6.5558(4)	6.6469(4)	12.2394(6)	$\beta = 102.844(3)°$	01F1
α-$Tb_2Si_2O_7$(B)	$P\bar{1}$-P1	6.623(5)	6.684(5)	12.101(9)	$\alpha = 93.97(7)°$ $\beta = 89.85(9)°$ $\gamma = 91.55(6)°$	70F1
δ-$Tb_2Si_2O_7$(E)	Pnam-$Pna2_1$	13.797(2)	5.036(1)	8.200(2)		70F1
α-$Dy_2Si_2O_7$(B)	$P\bar{1}$	6.6158(2)	6.6604(2)	12.0551(4)	$\alpha = 94.373(2)°$ $\beta = 90.836(2)°$ $\gamma = 91.512(2)°$	00F1
α-$Dy_2Si_2O_7$(B)	$P\bar{1}$-P1	6.639(2)	6.691(2)	12.152(3)	$\alpha = 94.03(3)°$ $\beta = 89.81(2)°$ $\gamma = 91.69(3)°$	70F1

Table 3 (continued)

Silicate	Space group	Lattice parameters				Refs.
		a [Å]	*b* [Å]	*c* [Å]	α, β, γ	
δ-$Dy_2Si_2O_7$(E)	Pnam-$Pna2_1$	13.7275(9)	5.0303(3)	8.2050(6)		70F1
δ-$Dy_2Si_2O_7$(E)	Pnam-$Pna2_1$	13.713(9)	5.036(4)	8.207(7)		82A1
δ-$Dy_2Si_2O_7$(E)	$Pna2_1$	13.740(15)	5.012(5)	8.26(1)		70S2
α-$Ho_2Si_2O_7$(B)	$P\bar{1}$-P1	6.664(5)	6.674(5)	12.110(9)	α = 94.07(8)° β = 89.97(8)° γ = 91.66(7)°	70F1
β-$Ho_2Si_2O_7$(C)	C2/m-C2-Cm	6.875(5)	9.184(9)	4.697(4)	β = 101.69(6)°	70F1
β-$Ho_2Si_2O_7$(C)	C2/m	6.89	8.98	4.72	β = 101.8°	68I1
δ-$Ho_2Si_2O_7$(E)	$Pna2_1$	13.700(15)	4.980(5)	8.23(1)		70S2
δ-$Ho_2Si_2O_7$(E)	Pnam-$Pna2_1$	13.7934(9)	5.0371(4)	8.2524(8)		70F1
δ-$Ho_2Si_2O_7$(E)	Pnam-$Pna2_1$	13.645(5)	5.016(2)	8.143(4)		82A1
γ-$Ho_2Si_2O_7$(D)	$P2_1$/b	4.686(5)	5.580(5)	10.84(2)	β = 95°58(10)′	70S2
γ-$Ho_2Si_2O_7$(D)	$P2_1$/a	5.957(2)	10.842(3)	4.696(2)	α = 90.0° β = 95.72(3)° γ = 90.0°	70F1
α-$Er_2Si_2O_7$(B)	$P\bar{1}$-P1	6.583(5)	6.609(5)	12.000(9)	α = 94.50(8)° β = 90.57(8)° γ = 91.79(9)°	70F1
β-$Er_2Si_2O_7$(C)	C2/m-C2-Cm	6.841(5)	9.135(9)	4.694(6)	β = 101.70(7)°	70F1
β-$Er_2Si_2O_7$(C)	C2/m	6.85	8.94	4.72	β = 101.6°	68I1
γ-$Er_2Si_2O_7$(D)	$P2_1$/a	5.588(2)	10.793(3)	4.689(2)	α = 90.0° β = 95.82° γ = 90.0°	70F1
γ-$Er_2Si_2O_7$(D)	$P2_1$/a	5.557(1)	10.803(9)	4.684(2)	β = 96.02(3)°	82A1
γ-$Er_2Si_2O_7$(D)	$P2_1$/b	4.683(5)	5.556(5)	10.79(1)	β = 96.00°(10)′	70S2
α-$Tm_2Si_2O_7$(B) (high pressure)	$P\bar{1}$-P1	6.548(10)	6.576(10)	11.92(2)	α = 85.61(20)° β = 91.19(20)° γ = 89.19(20)°	77B1
β-$Tm_2Si_2O_7$(C)	C2/m-C2-Cm	6.818(7)	9.104(9)	4.679(5)	β = 101.75(8)°	70F1
β-$Tm_2Si_2O_7$(C)	C2/m-C2-Cm	6.819(9)	8.871(9)	4.730(8)	β = 101.46(8)°	82A1
β-$Tm_2Si_2O_7$(C)	C2/m	6.824(10)	8.91(1)	4.704(5)	β = 101°50(10)′	70S2
β-$Tm_2Si_2O_7$(C)	C2/m	6.82	8.90	4.71	β = 101.9°	68I1
γ-$Tm_2Si_2O_7$(D)	$P2_1$/a	5.543(5)	10.78(1)	4.680(5)	β = 96.10(10)°	77B1
$Tm_2Si_2O_7$(X)	tetragonal	6.594(5)		12.00(1)		77B1
α-$Yb_2Si_2O_7$(B)	$P\bar{1}$-P1	5.532(10)	6.555(1)	11.89(2)	α = 85.72(20)° β = 91.15(20)° γ = 88.21(20)°	77B1
β-$Yb_2Si_2O_7$(C)	C2/m	6.81	8.88	4.71	β = 102°	68I1
β-$Yb_2Si_2O_7$(C)	C2/m	6.802(5)	8.875(10)	4.703(5)	β = 102°07(10)′	70S1
β-$Yb_2Si_2O_7$(C)	C2/m-C2-Cm	6.789(6)	9.067(9)	4.681(4)	β = 101.84(7)°	70F1
β-$Yb_2Si_2O_7$(C)	C2/m-C2-Cm	6.764(8)	8.827(8)	4.716(6)	β = 102.02(8)°	82A1
γ-$Yb_2Si_2O_7$(D)	$P2_1$/a	5.516(5)	10.70(1)	4.678(5)	β = 96.17(10)°	77B1
$Yb_2Si_2O_7$(X)	tetragonal	6.574(5)		11.99(1)		77B1

Table 3 (continued)

Silicate	Space group	Lattice parameters				Refs.
		a [Å]	*b* [Å]	*c* [Å]	α, β, γ	
α-$Lu_2Si_2O_7$(B) (high pressure)	$P\bar{1}$-P1	6.514(10)	6.539(10)	11.84(2)	α= 85.60(20)° β= 91.47(20)° γ= 88.16(20)°	77B1
α-$Lu_2Si_2O_7$(B)[14)]	$P\bar{1}$-P1	6.479	6.508	11.795	α= 85.54° β= 90.61° γ= 87.42°	77B1
β-$Lu_2Si_2O_7$(C)	C2/m	6.78	8.84	4.71	β= 101.9°	68I1
β-$Lu_2Si_2O_7$(C)	C2/m-C2-Cm	6.760(6)	9.051(9)	4.685(7)	β= 101.86(6)°	70F1
β-$Lu_2Si_2O_7$(C)	C2/m-C2-Cm	6.748(8)	8.836(8)	4.723(6)	β= 101.83(7)°	82A1
β-$Lu_2Si_2O_7$(C)	C2/m	6.78	8.84	4.71	β= 101.9°	68I1
β-$Lu_2Si_2O_7$(C)		6.7655(5)	8.8369(6)	4.7121(3)	β= 102.00(6)°	70S1
β-$Lu_2Si_2O_7$[7)](C)	C2/m	6.7665(14)	8.8407(18)	4.7195(27)	β= 101.95(3)°	81B1
β-$Lu_2Si_2O_7$(C)		6.773(1)	8.842(2)	4.715(1)	β= 101.95(1)°	81O1
γ-$Lu_2Si_2O_7$(D)	$P2_1/a$	5.494(5)	10.66(1)	4.688(5)	β= 96.19(10)°	77B1
$Lu_2Si_2O_7$(X)	tetragonal	6.565(5)		11.95(1)		77B1
β-$Y_2Si_2O_7$[8)](C)	C2/m	6.83	8.89	4.72	β= 101.7°	67B2
β-$Y_2Si_2O_7$(C)	C2/m	6.90	8.89	4.72	β= 101.7°	68I1
γ-$Y_2Si_2O_7$(D)	$P2_1/c$	4.694(1)	10.856(5)	5.588(1)	α= 90° β= 96.01(3)°	99L1
γ-$Y_2Si_2O_7$(E)	$P2_1/b$	4.663(5)	5.536(5)	10.784(21)	β= 96°06′	70S2
δ-$Y_2Si_2O_7$(E)	$Pna2_1$	13.69(2)	5.020(5)	8.165(10)		70S2
δ-$Y_2Si_2O_7$[10)](E)	Pnam-$Pna2_1$	13.680(6)	5.013(2)	8.141(4)		82A1
δ-$Y_2Si_2O_7$[10)](E)	Pnam	13.655(5)	5.016(3)	8.139(3)		90D1
y-$Y_2Si_2O_7$	monoclinic	7.50(3)	8.06(3)	5.02(2)	β= 112°00(30)′	72B1
y-$Y_2Si_2O_7$	Aba2	8.06	9.34	6.92		88D1
β-$In_2Si_2O_7$	C2/m	6.63	8.63	4.69	β= 102.8°	68I1
β-$In_2Si_2O_7$	C2/m	6.622(2)	8.600(2)	4.699(1)	β= 102.89(2)°	81O1
$In_2Si_2O_7$[6)]	Fd3m	9.413(3)				77R1
$Na_3ScSi_2O_7$	Pbnm	5.354(3)	9.347(4)	13.089(4)		73F1
$Sm_4S_3Si_2O_7$	$I4_1/amd$	11.839(5)		13.928(5)		82S1
$La_4Se_3Si_2O_7$	$I4_1/amd$	12.2846(18)		14.6992(10)		93D1
$Ag_6Si_2O_7$	P2/n	10.264(4)	5.259(3)	8.052(4)	β= 110.5(1)°	77J1
Keiviite[11)]	C2/m	6.840(2)	8.916(4)	4.745(1)	β= 102.11(3)°	83V1, 84D1
Gittinsite[12)]	C2/m	6.878(4)	8.674(4)	4.697(2)	β= 101.74(4)°	80A1
Gittinsite[13)]	C2	6.852(2)	8.659(1)	4.686(2)	β= 101.69(2)°	89R1

Table 3 (continued)

[1] $Mn_{0.030}Dy_{0.023}Er_{0.027}Tm_{0.009}Yb_{0.111}Lu_{0.026}Hf_{0.008}Y_{0.490}Zr_{0.058}Ca_{0.011}Sc_{1.132}Mg_{0.020}Fe_{0.081}Si_{1.950}Al_{0.037}O_7$;
[2] $Mn_{0.054}Dy_{0.015}Er_{0.008}Tm_{0.001}Yb_{0.038}Lu_{0.007}Hf_{0.014}Y_{0.223}Zr_{0.102}Ca_{0.011}Sc_{1.385}Mg_{0.024}Fe_{0.113}Si_{1.958}Al_{0.051}O_7$;
[3] $Mn_{0.018}Dy_{0.07}Er_{0.014}Tm_{0.003}Yb_{0.066}Lu_{0.015}Hf_{0.001}Y_{0.213}Zr_{0.040}Ca_{0.007}Sc_{1.548}Mg_{0.005}Fe_{0.060}Si_{1.963}Al_{0.049}O_7$;
[4] composition not mentioned; natural sample
[5] SiO_2 45.45 %; Sc_2O_3 42.06 %; Y_2O_3 8.89 %; Fe_2O_3 2.83 %; BeO 0.51 %; ign 0.59 %;
[6] Prepared at 1200 °C and 120 kbar;
[7] Reid, A.F. (private communication) cited by [77B1];
[8] Prepared at 1225°…1445 °C;
[9] Prepared at 1445…1535 °C;
[10] Prepared at $T > 1535$ °C;
[11] $(Yb_{1.43}Lu_{0.23}Er_{0.17}Tm_{0.08}Y_{0.05}Dy_{0.03}Ho_{0.02})Si_{1.99}O_7$;
[12] $Ca_{0.98}Zr_{0.98}Si_{2.03}O_7$;
[13] CaO 18.4 %; ZrO_2 40.3 %,SiO_2 40.8 %;
[14] Data of Reid, A.F. (unpublished); cited by [77B1].

Table 4. γ-$Er_2Si_2O_7$. The interaction energies (in cm^{-1}) between an ion in sublattice I with ions in sublattices n [86L1].

Interaction energy	Sublattice number, n			
	1	2	3	4
Total	0.229	–0.371	–1.431	–0.700
Dipole	0.437	–0.193	–0.315	–0.352
Exchange	–0.208	–0.178	–1.116	–0.248

Table 5. Data obtained by ^{29}Si NMR measurements.

Silicate	[00P1]			[87S1]	[84G1]	[88D2]		[89H1]	
	Thermal treatment	δ_{iso} [1] [ppm]	*DH* [2] [Hz]	δ_{iso} [ppm]	δ_{iso} [ppm]	δ_{iso} [ppm]	*DH* [Hz]	δ_{iso} [ppm]	*DH* [Hz]
α-$Y_2Si_2O_7$	SG[3], 1200 °C, 24 h, I[4], Q[5]	–80.96	21	–83.4					
		–82.43	20						
		–83.41	20						
		–84.95	20						
β-$Y_2Si_2O_7$	SG[3], 1350 °C, 24 h, I[4], Q[5]	–93.65	14	–93.6					
γ-$Y_2Si_2O_7$	MP[6], 1400 °C, 6 h	–92.68	13	–92.8	–92.9	–92.8	~ 50		
δ-$Y_2Si_2O_7$	MP[6], 1700 °C, 2 h	–81.27	14	–81.2[7]	–81.6[7]				
		–83.00	15	–82.9[7]	–83.5[7]				
y-$Y_2Si_2O_7$	SG[2], 900 °C, 24 h	–83.0[7]							
β -$La_2Si_2O_7$								–83.8	≅ 200

[1] relative to tetramethylsilane; [2] Full width half height; [3] Sol-gel method; [4] Isothermal calcination; [5] quench in air; [6] mixed powder route; [7] poor signal to noise ratio.

Table 6. Refractive indices.

Sample	n_α	n_β	n_γ	$2V_a$	Optical sign	Refs.
Keiviite[11)]	1.723	1.758	1.768	58°	–	83V1, 84D1
Gittinsite[12)]	1.720(2)	1.736(2)	1.738(2)	30(10)°		80A1
$La_2Si_2O_7$	1.776	1.770	1.776		+	82A1
$Ce_2Si_2O_7$	1.789	1.784	1.782		+	82A1
$Pr_2Si_2O_7$	1.790	1.783	1.781		+	82A1
$Nd_2Si_2O_7$	1.794	1.785	1.783		+	82A1
$Gd_2Si_2O_7$	1.777	1.765	1.763		+	82A1
$Dy_2Si_2O_7$	1.784	1.766	1.762		+	82A1
$Ho_2Si_2O_7$	1.776	1.769	1.761		–	82A1
$Er_2Si_2O_7$	1.782	1.773	1.728		–	82A1
$Tm_2Si_2O_7$	1.778	1.756	1.721		–	82A1
$Yb_2Si_2O_7$	1.776	1.757	1.718		–	82A1
$Lu_2Si_2O_7$	1.765	1.754	1.713		–	82A1
$Y_2Si_2O_7$	1.753	1.746	1.736		–	82°1
$Sc_2Si_2O_7$	1.810	1.792	1.749		–	82A1

[11, 12)] composition is given in Table 3.

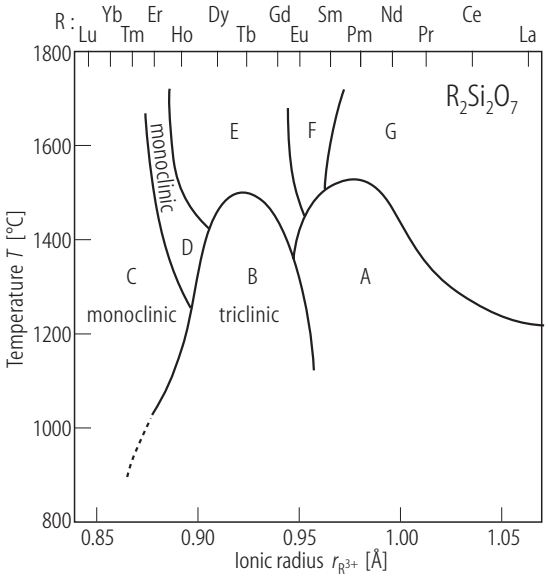

Fig. 1. $R_2Si_2O_7$. Polymorphism at atmospheric pressure [70F1].

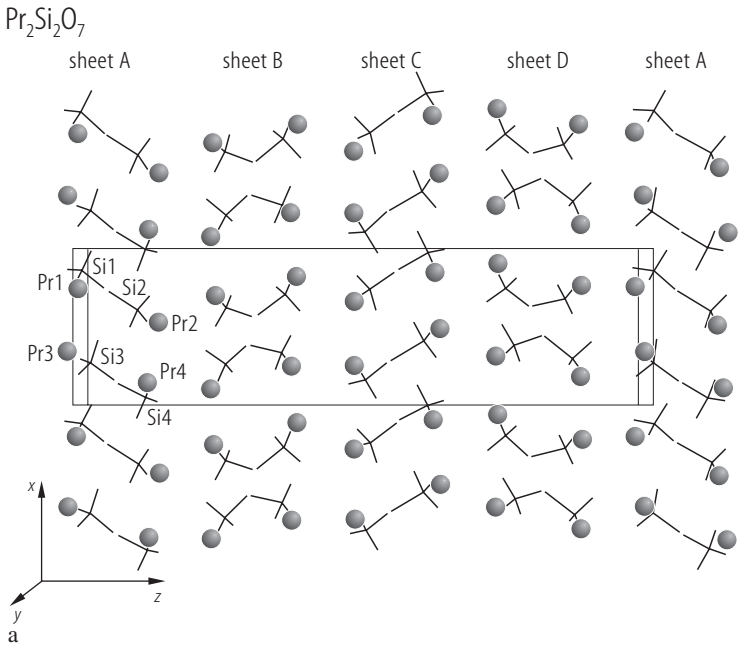

Fig. 2a. For caption see p. 21.

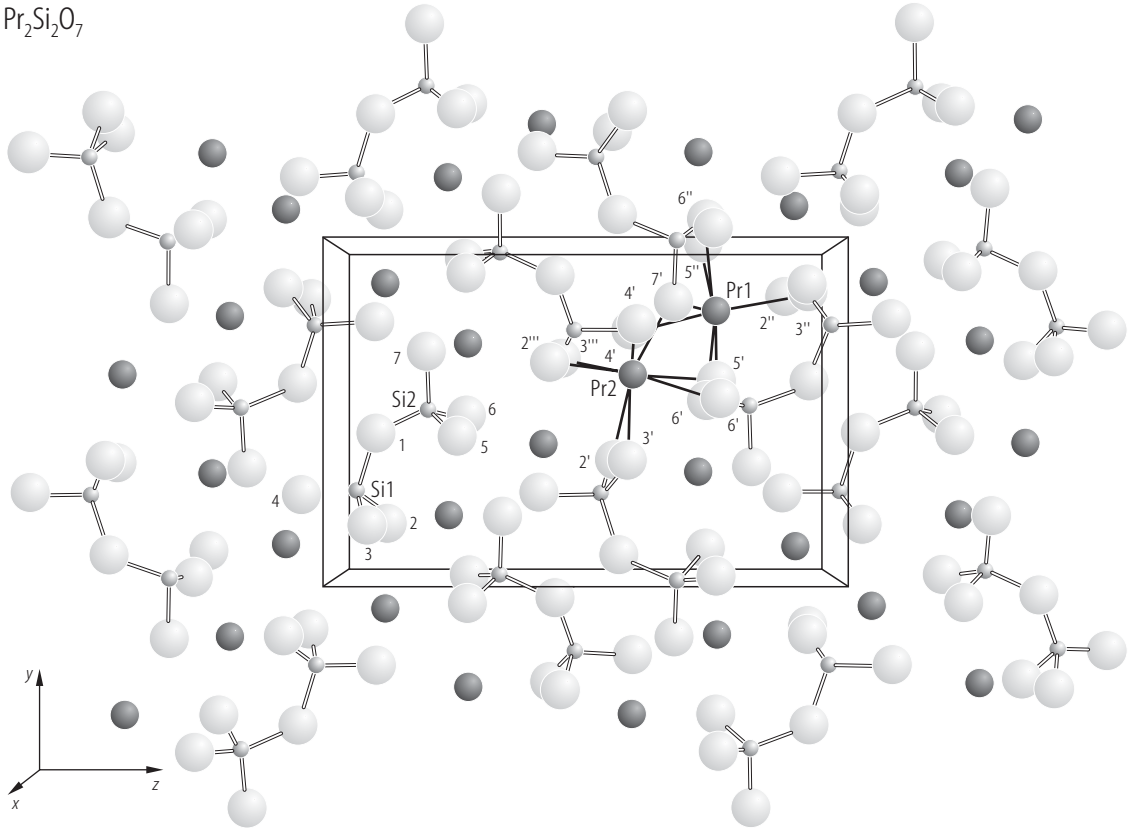

b

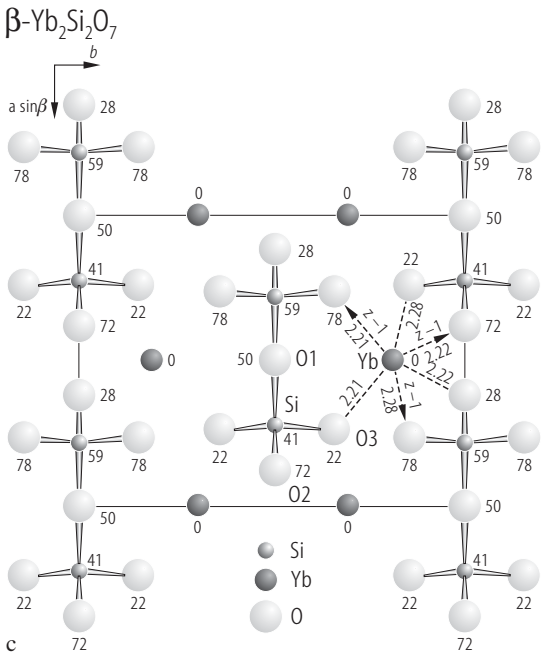

c

Figs. 2b,c. For caption see p. 21.

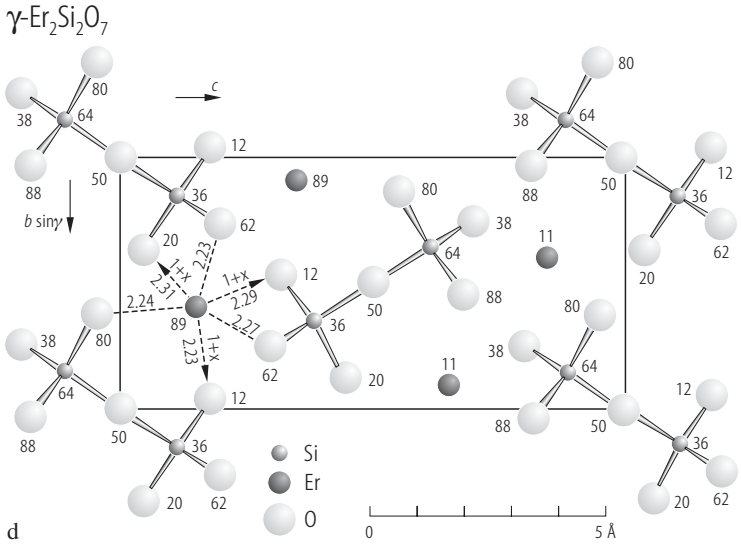

d

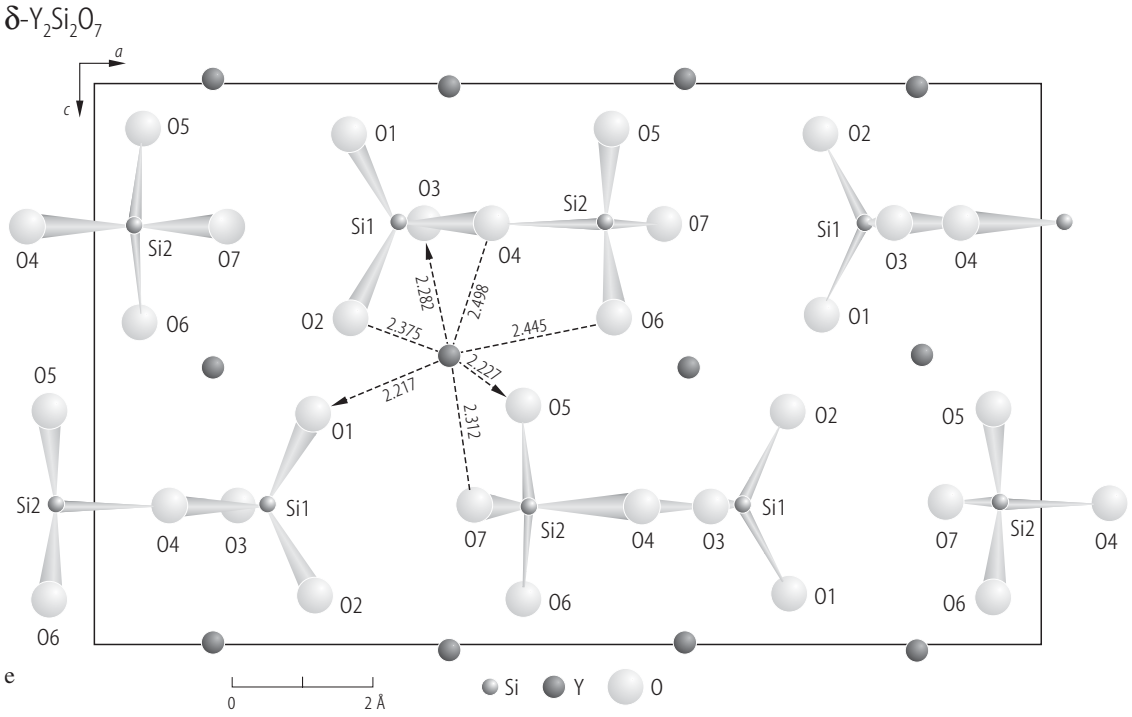

e

Figs. 2d, e. For caption see p. 21.

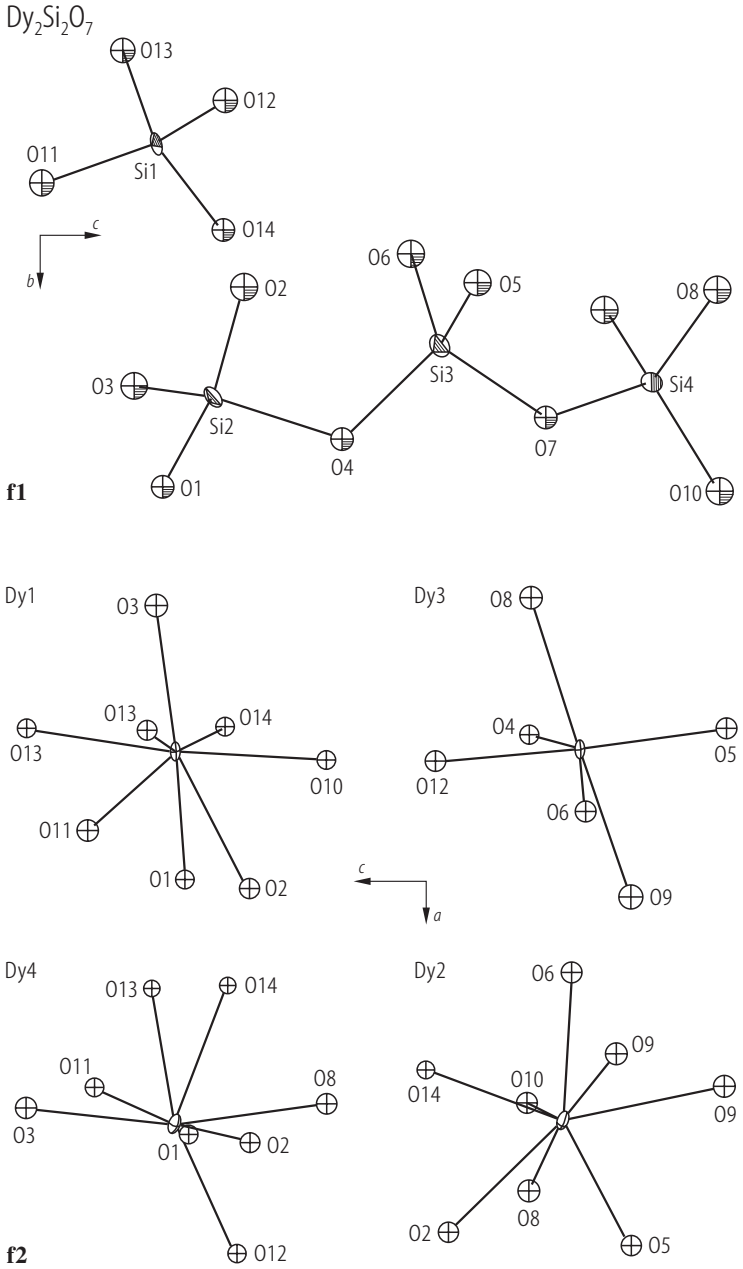

Fig. 2f. For caption see p. 21.

$Nd_2Si_2O_7$

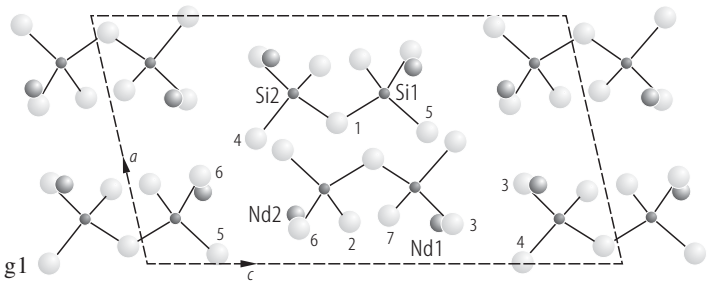

g1

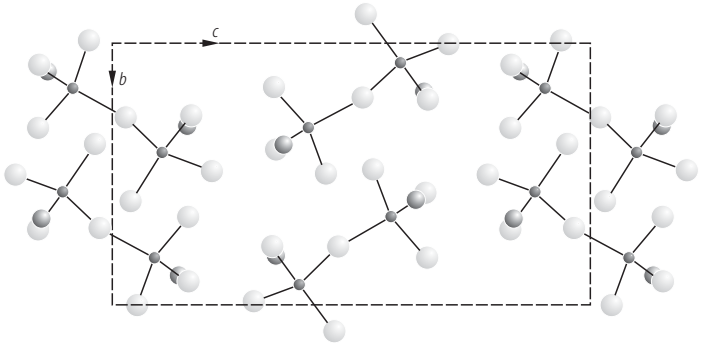

g2

Fig. 2. $R_2Si_2O_7$ crystal structures. **(a)** R = Pr (A-type) projected along [010]. Dark spheres represent Pr atoms at different levels. Si–O bond skeletons of the $[Si_2O_7]^{6-}$ double tetrahedra are shown only [71F1]; **(b)** R = Pr (G-type), perspective view of the pseudo-orthorhombic structure along [100] in the setting after space group $P2_1/n$. In order to compare the figure with the data from Table 2, the coordinates *x*, *y*, *z* after $P2_1/c$ have to be transformed to *x*–*z*, *y*, *z* for $P2_1/n$. Dark spheres represent Pr atoms. Numbers n of oxygen symbols, On, are given merely [71F1]; **(c)** R = Yb (β(C)-type) structure projected along ***c***-axis [70S2]; **(d)** R = Er (γ(D)-type) projected along ***a***-axis [70S2]; **(e)** $Y_2Si_2O_7$ (δ(E)-type) projected on (010). Dashed lines are Y–O contacts and the arrow-heads indicate O above the plane of the sheet [90D1]; **(f)** $Dy_2Si_2O_7$ (B-type): **(f1)** linear triple tetrahedral group $[Si_3O_{10}]$ and isolated $[SiO_4]$ tetrahedron; ***a****-axis projection, **(f2)** coordination of Dy sites; [010] projection. Thermal ellipsoids for Si and Dy atoms are scaled to enclose 50 % probability [00F1]; **(g)** $Nd_2Si_2O_7$ (K-type): **(g1)** (010) projection, **(g2)** [100] projection [01F1]. In **(c)** and **(d)** *z* and *x* coordinates (×100) are shown, in **(c)**, **(d)**, **(e)** some distances from Er, Yb andY, respectively, to oxygen atoms are given (in Å).

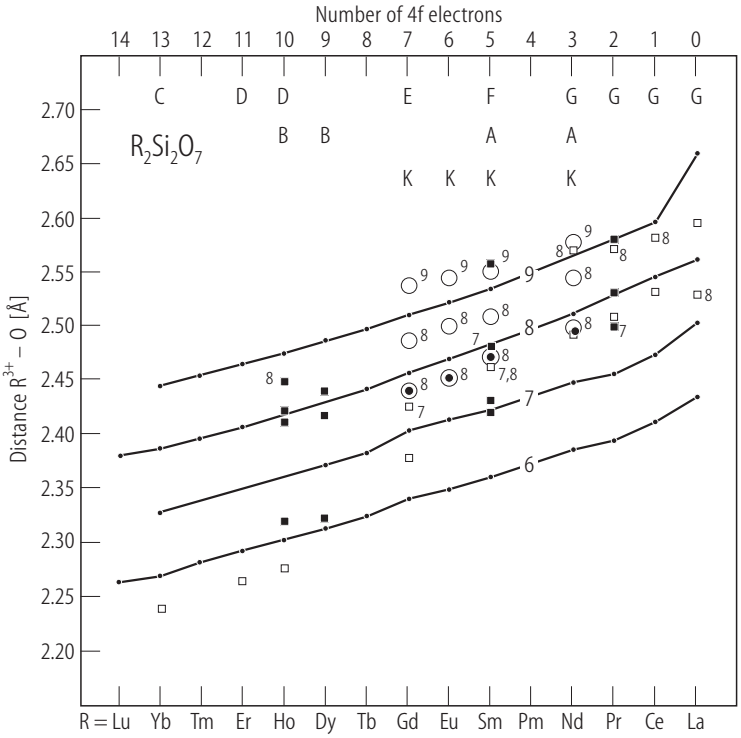

Fig. 3. $R_2Si_2O_7$ disilicates. Mean R–O bond distances of non-equivalent polyhedra, relative to the sum of the effective cation-anion radii for coordination numbers 6, 7, 8 and 9 [76S1]. Open squares are structures of high-temperature phases (top row of structure-type labels) and full squares are structures of moderate-temperature phases. Subscripts and superscripts are coordination numbers [00F1, 01F1].

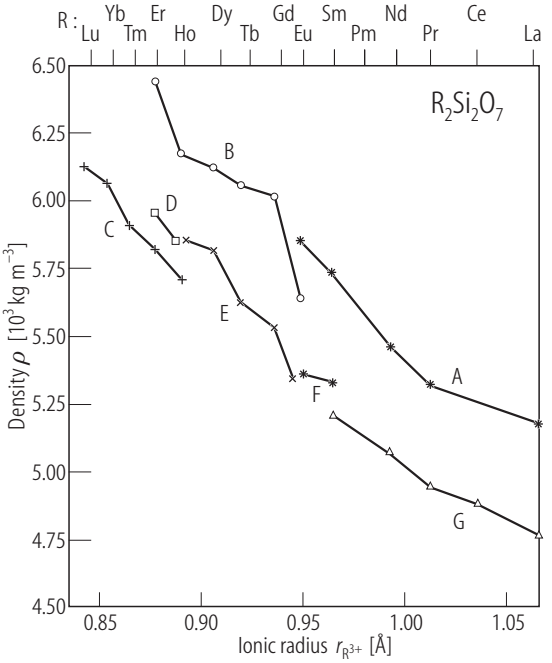

Fig. 4. $R_2Si_2O_7$. Densities for some structure types [70F1, 77B1].

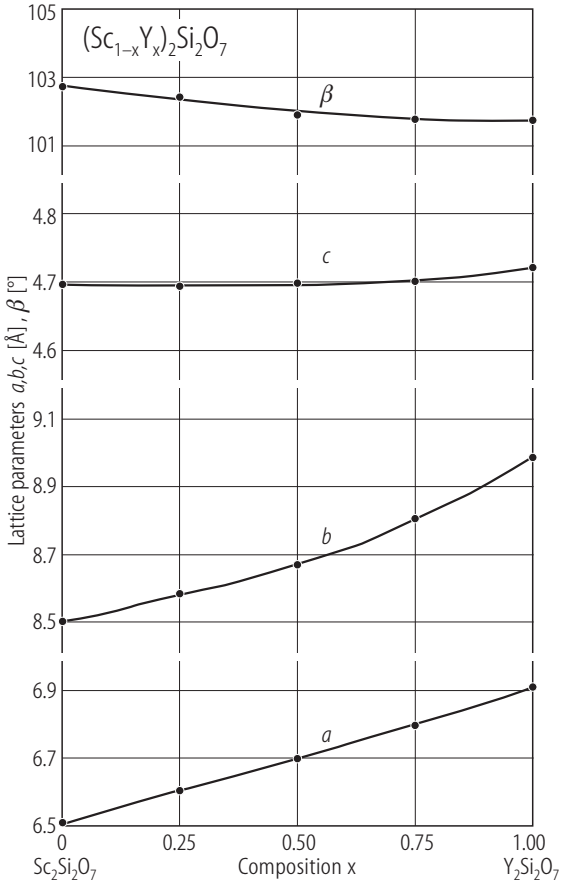

Fig. 5. $(Sc_{1-x}Y_x)_2Si_2O_7$. Composition dependences of lattice parameters [68I1].

→

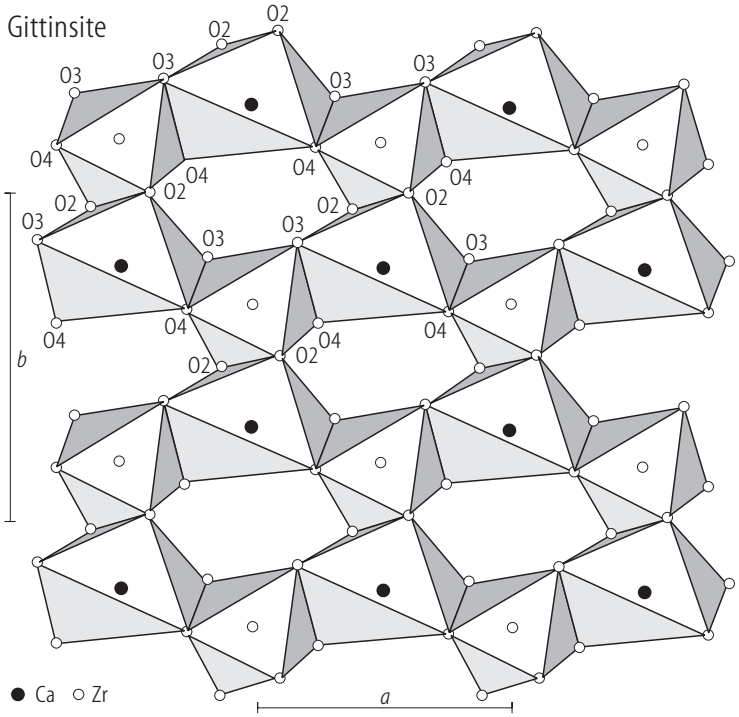

Fig. 6. Gittinsite. A (001) projection of the layer of octahedra [89R1].

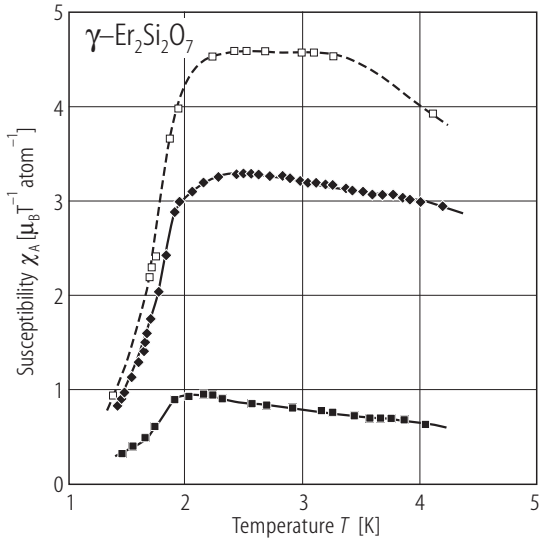

Fig. 7. γ-$Er_2Si_2O_7$ (D). Magnetic susceptibilities as function of temperature in the range 1.4…4.2 K for the principal axes: (■): ***c***-axis; (♦): ***a***-axis; (□): ***m***-axis [86L1].

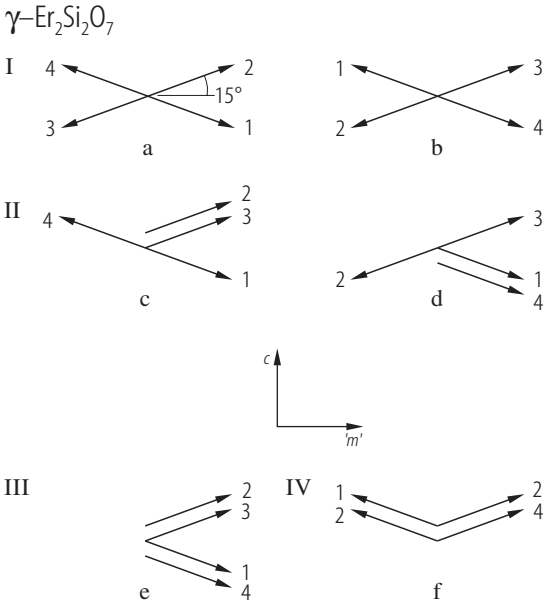

Fig. 8. γ-$Er_2Si_2O_7$ (D). Possible four sublattice magnetic arrangements under applied fields of varying strength and direction. **(a)**, **(b)** (sublattice I) Equivalent arrangements in zero field; **(c)**, **(d)** (sublattice II) possible intermediate configurations; **(e)** (sublattice III), **(f)** (sublattice IV) configurations corresponding to saturation moments in strong field parallel to ***m***- and ***c***-directions, respectively [86L1].

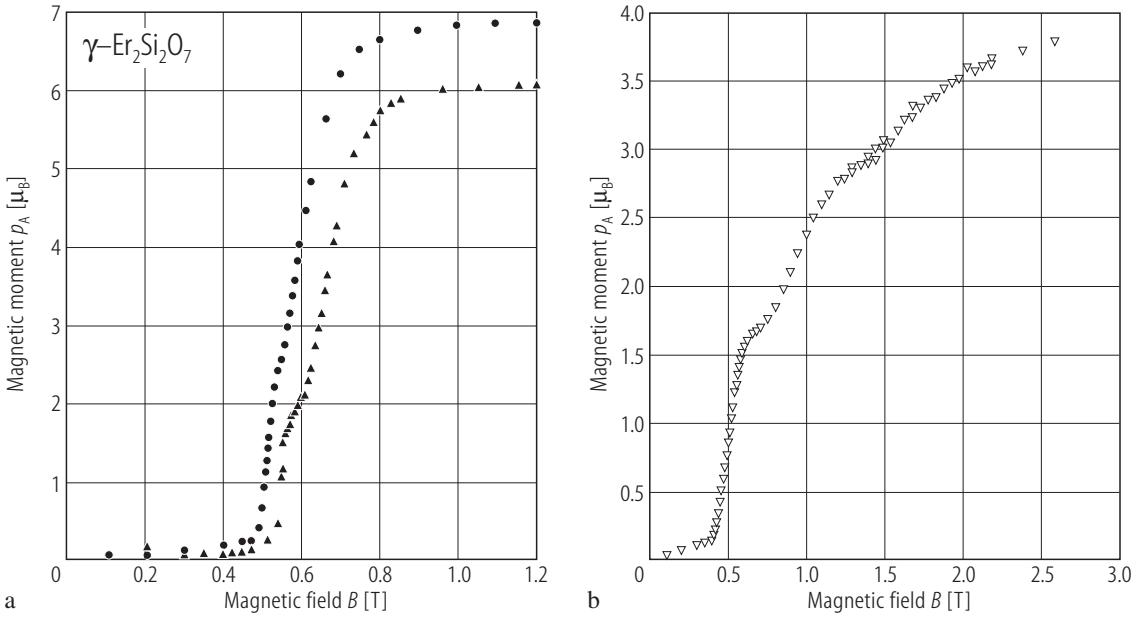

Fig. 9. γ-$Er_2Si_2O_7$ (D). Magnetic moments per atom as function of external field, at 0.5 K, for fields applied: **(a)** parallel to ***a***-(▲) and ***m***-axis (●) and **(b)** at 55° from ***m***-axis in the (***m***,***c***) plane [86L1].

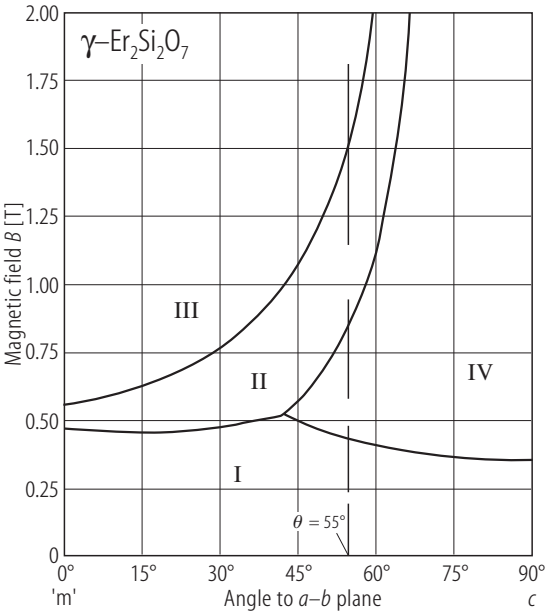

Fig. 10. γ-$Er_2Si_2O_7$ (D) the phase diagram at T = 0 K as a function of external field direction in the (***m***,***c***) plane. The phases I to IV correspond to the magnetic moment configurations shown in Fig. 8: I-**(a)**, **(b)**; II-**(c)**, **(d)**; III-**(e)**; IV-**(f)** [86L1].

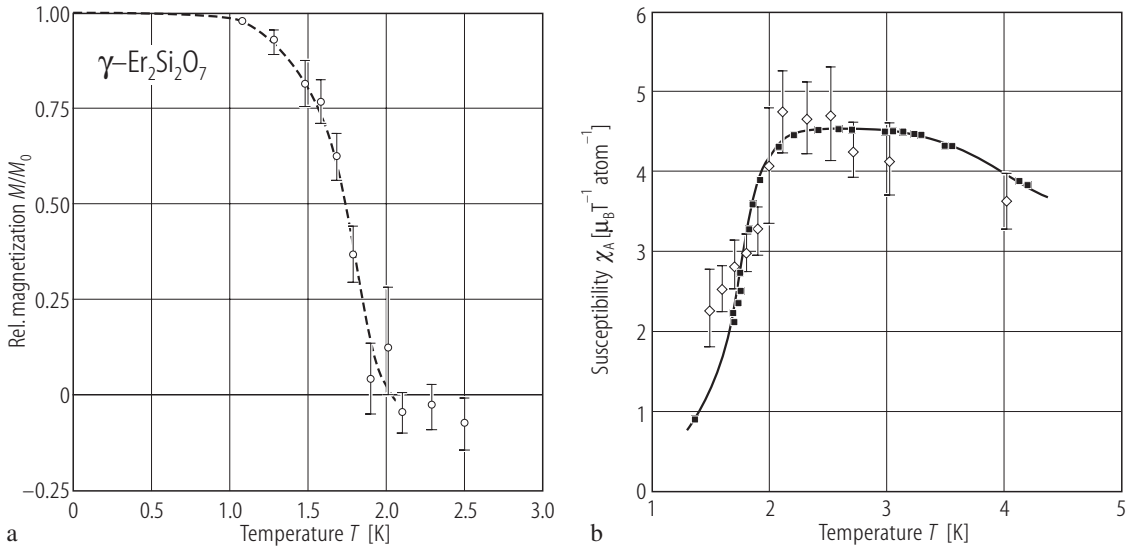

Fig. 11. γ-$Er_2Si_2O_7$ (D). **(a)** Calculated Er reduced sublattice magnetization versus temperature (○). The broken curve corresponds to a molecular field prediction for $S = 1/2$. **(b)** Temperature dependence of the magnetic susceptibility along the ***m***-direction (■ - experimental values, ◊ calculated data) [86L1].

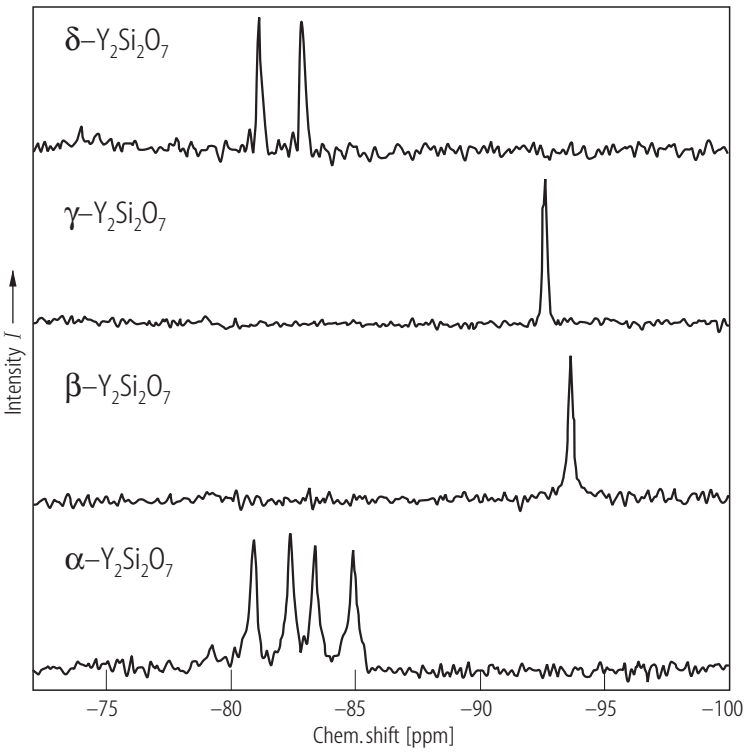

Fig. 12. α-$Y_2Si_2O_7$; β-$Y_2Si_2O_7$; γ-$Y_2Si_2O_7$; δ-$Y_2Si_2O_7$: ^{29}Si MAS NMR spectra; 72, 1, 4 and 44 transients were recorded with 300, –, 600 and 300 s as recycle delays, respectively [00P1].

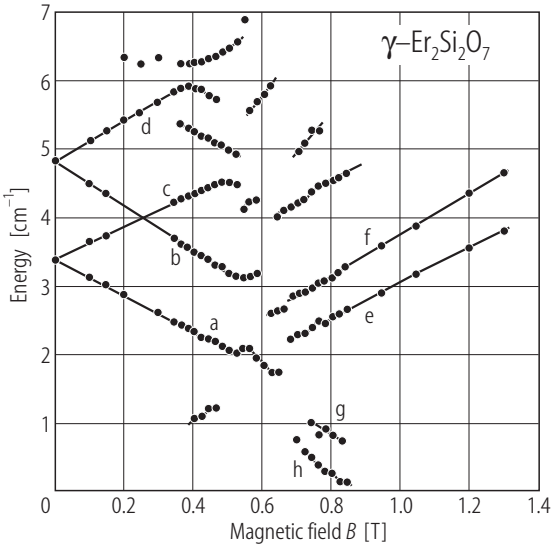

Fig. 13. γ-$Er_2Si_2O_7$ (D). Zeeman spectra of Er^{3+} ($^4I_{15/2}GS \rightarrow {}^4S_{3/2}$ lower component) as function of applied field parallel to the ***m***-axis, at 0.7 K. The energy (cm^{-1}) is given relative to a baseline of 18200 cm^{-1} [86L1]. For lines a…h see text.

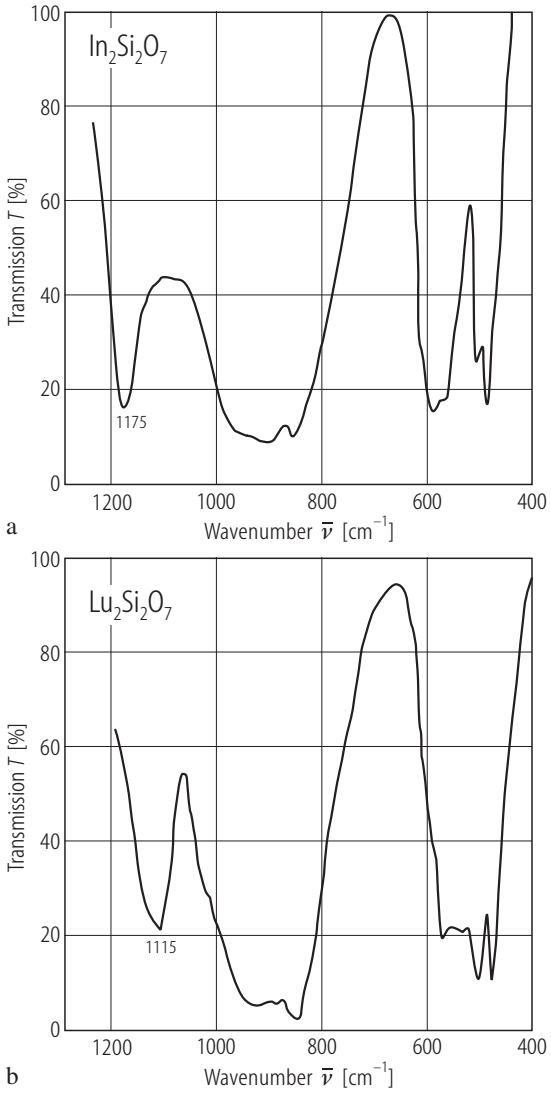

Fig. 14. $Lu_2Si_2O_7$, $In_2Si_2O_7$. Infrared absorption spectra [81O1].

References for 8.1.2.1

30Z1 Zachariasen, W.H.: Z. Kristallogr. 73 (1930) 1
61L1 Lazarev, A.N., Tenisheva, T.F.: Izv. Akad. Nauk SSSR Otd. Khim. Nauk 6 (1961) 964
62C1 Cruickshank, D.W.J., Lynton, H., Barclay, G.A.: Acta Crystallogr. 15 (1962) 491
62L1 Lazarev, A.N., Tenisheva, T.F., Bondar, I.A., Koroleva, L.N.: Izv. Akad. Nauk SSSR, Otd. Khim. Nauk 4 (1962) 557
62P1 Protosenko, E.G.: Zap. Vses. Mineral. Ova. 91 (1962) 260
64L1 Lazarev, A.N., Tenisheva, T.F.: Izv. Akad. Nauk SSSR, Otd. Khim. Nauk 3 (1964) 403
64W1 Warshaw, I., Roy, R.: Progress in Science and Technology of the Rare Earths, vol. 1, Pergamon, New York, 1964, p. 215
65K1 Knop, O., Brisse, F., Castellitz, L., Sutarno, I.: Can. J. Chem. 43 (1965) 2812
65L1 Lazarev, A.N., Tenisheva, T.F., Bondar, I.A.: Izv. Akad. Nauk SSSR, Neorg. Mater. 1 (1965) 1207
65T1 Tarte, P.: Acad. R. Belg. Cl. Sci. Mem. Collect. 35 (1965) 4a
65T2 Toropov, N.A., Bondar, I.A., Sidorenko, G.A., Koroleva, L.N.: Izv. Akad. Nauk SSSR, Neorg. Mater. 1 (1965) 218
67B1 Batalieva, N.G., Pyatenko, Yu.A.: Zh. Strukt. Khim. 8 (1967) 548
67B2 Batalieva, N.G., Bondar, I.A., Sidorenko, G.A., Toropov, N.A.: Dokl. Akad. Nauk. SSSR Ser. Chem. 173 (1967) 339
67B3 Batalieva, N.G., Krivokoneva, G.K., Pyatenko, Yu.A.: Dokl. Akad. Nauk. SSSR Ser. Chem. 176 (1967) 1146
67S1 Smolin, Yu.I., Shepelov, Yu.F.: Izv. Akad. Nauk SSSR, Neorg. Mater. 3 (1967) 1034
68B1 Batalieva, N.G., Pyatenko, Yu.A.: Zh. Strukt. Khim. 9 (1968) 921
68B2 Bondar, L.A., Koroleva, L.N., Toropov, N.A.: in: Growth of Crystals, Vol. 6, Consultants Bureau, New York, 1968
68H1 Hoekstra, H.R., Siegel, S.: Inorg. Chem. 7 (1968) 141
68I1 Ito, J., Johnson, H.: Am. Mineral. 53 (1968) 1940
69B1 Batalieva, N.G., Krivokoneva, G.K., Bondar, I.A., Sidorenko, G.A.: Dokl. Akad. Nauk. SSSR Ser. Chem. 189 (1969) 615
69F1 Felsche, J.: J. Appl. Crystallogr. 2 (1969) 303
69F2 Felsche, J., Hirsiger, W.: J. Less Common Met. 18 (1969) 131
70B1 Bondar, I.A.: Colloq. Int. CNRS 180 (1970) 337
70F1 Felsche, J.: J. Less Common Met. 21 (1970) 1
70F2 Felsche, J.: Naturwissenschaften 57 (1970) 452
70F3 Felsche, J.: Naturwissenschaften 57 (1970) 669
70S1 Shannon, R.D., Prewitt, C.T.: J. Solid State Chem. 2 (1970) 199
70S2 Smolin, Yu.I., Shepelev, Yu.F.: Acta Crystallogr. B 26 (1970) 484
70S3 Smolin, Yu.I., Shepelev, Yu.F., Butikova, I.K.: Kristallografiya 15 (1970) 256 (Sov. Phys. Crystallogr. 15 (1970) 214)
71F1 Felsche, J.: Z. Kristallogr. 133 (1971) 364
71L1 Lazarev, A.N., Mirgorodskii, A.P.: Izv. Akad. Nauk SSSR, Neorg. Mater. 7 (1971) 1224
72B1 Batalieva, N.G., Pyatenko, Yu.A.: Kristallografiya 16 (1971) 905 (Sov. Phys. Crystallogr. 16 (1972) 786)
72F1 Felsche, J.: Naturwissenschaften 59 (1972) 35
72S1 Smolin, Yu.I., Shepelev, Yu.F., Titov, A.P.: Kristallografiya 17 (1972) 857
73F1 Felsche, J.: Struct. Bonding 13 (1973) 99
73L1 Leonov, A.J., Bondar, I.A.: Inorg. Mater. 9 (1973) 50
73S1 Smolin, Yu.I., Shepelev, Yu.F., Titov, A.F.: Kristallografiya 17 (1972) 857 (Sov. Phys. Crystallogr. 17 (1973) 749)
73T1 Tarte, P., Pottier, M.J., Procés, A.M.: Spectrochim. Acta 29A (1973) 1017
74W1 Wanklyn, B.M., Wondre, F.R., Ansell, G.B., Davison, W.: J. Mater. Sci. 9 (1974) 2007
76S1 Shannon, R. D.: Acta Crystallogr. A32 (1976) 751
77B1 Bocquillon, G., Chateau, C., Loriers, C., Loriers, J.: J. Solid State Chem. 20 (1977) 135
77J1 Jansen, M.: Acta Crystallogr. B33 (1977) 3584

77R1 Reid, A.F., Li, C., Ringwood, A.E.: J. Solid State Chem. 20 (1977) 219
78W1 Wanklyn, B.M.: J. Cryst. Growth 43 (1978) 336
79M1 Magsood, A., Wanklyn, B.M., Garton, G.: J. Cryst. Growth 46 (1979) 671
80A1 Ansell, H.G., Roberts, A.C., Plant, A.G., Sturman, B.D.: Can. Mineral 18 (1980) 201
81B1 Bretheau-Raynal, F., Lance, M., Charpin, P.: J. Appl. Crystallogr. 14 (1981) 349
81O1 Ohashi, H., Osawa, T.: J. Jpn. Assoc. Mineral. Petrol. Econ. Geol. 76 (1981) 368
82A1 Ananeva, G.V., Karapetyan, V.E., Korovkin, A.M., Merkulyaeva, T.I., Peschanskaya, I.A., Savinova, I.R., Feofilov, P.P.: Izv. Akad. Nauk. SSSR: Neorg. Mater. 18 (1982) 442
82S1 Siegrist, T., Petter, W., Hulllinger, F.: Acta Crystallogr. B 38 (1982) 2872
83V1 Veloshin, A.V., Pakhomovsky, Ya.A., Tyusheva, F.N.: Mineral. Zh. 5 (1983) 94
84D1 Dunn, P.J., Cabri, L.J., Ferraiolo, J.A., Grice, J.D., Jambor, J.L., Mueller, W., Shigley, J.E., Puziewicz, J., Vanko, D.A.: Am. Mineral. 69 (1984) 1190
84G1 Grimmer, A.R., Von Lampe, F., Mägi, M., Lippmaa, E.: Monatsh. Chem. 115 (1984) 561
86L1 Leask, M.J.M., Tapster, P.R., Wells, M.R.: J. Phys. C.: Solid State Phys. 19 (1986) 1173
86L2 Liddell, K., Thompson, D.P.: Br. Ceram. Trans. J. 85 (1986) 17
87D1 Dowty, E.: Phys. Chem. Miner. 14 (1987) 542
87S1 Smith, M.E.: PhD. Thesis, University of Warwick, 1987, cited in [00P1]
88B1 Bianchi, R., Pilati, T., Diella, V., Gramaccioli, C.M., Mannucci, G.: Am. Mineral. 73 (1988) 601
88D1 Dinger, T.R., Rai, R.S. Thomas, G.: J. Am. Ceram. Soc. 71 (1988) 236
88D2 Dupree, R., Lewis, M.H., Smith, M.E.: J. Am. Chem. Soc. 110 (1988) 1083
89H1 Harris, R.K., Leach, M.J., Thompson, D.P.: Chem. Mater. 1 (1989) 336
89R1 Roelsfsen-Ahl, J., Peterson, R.C.: Can. Mineral. 27 (1989) 703
90D1 Dias, H.W., Glasser, F.P., Gunwardane, R.P., Howie, R.A.: Z. Kristallogr. 191 (1990) 117
91G1 Greis, O., Bossemeyer, H.G., Greil, P., Breidenstein, B., Haase, A.: Mater. Sci. For. 79-82 (1991) 803
91K1 Kruppa, D., Dupree, R., Lewis, M.H.: Mater. Lett. 11 (1991) 195
91N1 Nickel, E.H., Nichols, M.C.: Mineral Reference Manual, Van Nostrand Reinhold, 1991
93D1 Deudon, C., Meerschaut, A., Rouxel, J.: J. Solid State Chem. 104 (1993) 282
93T1 Thompson, D.P.: Mater. Res. Soc. Symp. Proc. 287 (1993) 79
94C1 Christensen, A.N.: Z. Kristallogr. 209 (1994) 7
94C2 Christensen, A. N., Hazell, R.G., Hewat, A.W.: Acta Chem. Scand. 51 (1994) 37
97C1 Christensen, A.N., Hazell, R.G., Hewat, A.W.: Acta Chem. Scand. 51 (1997) 37
97C2 Christensen, A. N., Jensen, A. F., Themsen, B. K., Hazell, R. G., Hanfland, M., Dooryhee, E.: Acta Chem. Scand. 51 (1997) 1178
97L1 Liddell, K., Thompson, D.P.: J. Mater. Sci. 32 (1997) 887
98I1 Izhevskii, V. A.: Powder Metall. Metal. Cer. 37 (1998) 67
99L1 Leonyuk, N.I., Belokoneva, E.L., Bocelli, G., Righi, L., Shranskii, E.V., Henrykhson, R.V., Kulman, N.V., Kozhbakhteeva, D.E.: J. Cryst. Growth 205 (1999) 361
00F1 Fleet, M.E., Liu, X.: Acta Crystallogr. B56 (2000) 940
00P1 Parmentier, J., Bodart, P.R., Audoin, L., Massouras, G., Thompson, D.P., Harris, R.K., Goursat, P., Besson, J.L.: J. Solid State Chem. 149 (2000) 16
01F1 Fleet, M.E., Liu, X.: J. Solid State Chem. 161 (2001) 166